APFoam-1.0: integrated CFD simulation of O₃–NOₓ–VOCs chemistry and pollutant dispersion in typical street canyon

Luolin Wu[1], Jian Hang[1], Xuemei Wang[2], Min Shao[2], and Cheng Gong[3]

[1]School of Atmospheric Sciences, Sun Yat-sen University, Guangzhou 510275, P. R. China
5 [2]Institute for Environmental and Climate Research, Jinan University, Guangzhou 510632, P. R. China
[3]China Aerodynamics Research and Development Center, Mianyang 621000, P. R. China

Correspondence to: Xuemei Wang (eciwxm@jnu.edu.cn) and Jian Hang (hangj3@mail.sysu.edu.cn)

Abstract. Urban air quality issues are closely related to the human health and economic development. In order to improve the resolution and numerical accuracy of urban air quality simulation, this study has developed the Atmospheric Photolysis

10 calculation framework (APFoam-1.0), an open-source CFD code based on OpenFOAM, which can be used to examine the micro-scale reactive pollutant formation and dispersion in the urban area. The chemistry module of the newly APFoam has been modified by adding five new types of reaction, which implements the coupling with atmospheric photochemical mechanism (full O₃–NOₓ–VOCs chemistry) and CFD model. Additionally, numerical model has been validated and shows the good agreement with wind tunnel experimental data, indicating that the APFoam has sufficient ability to study urban

15 turbulence and pollutant dispersion characteristics. By applying the APFoam, O₃–NOₓ–VOCs formation processes and dispersion of the reactive pollutants are analyzed in an example of typical street canyon (aspect ratio *H/W*=1). Chemistry mechanism comparison shows that O₃ and NO₂ are underestimated while NO is overestimated if the VOCs reactions are not considered in the simulation. Moreover, model sensitivity cases reveal that 82%–98% and 75%–90% of NO and NO₂ are related to the local vehicle emissions which are verified as the dominated contributors to local reactive pollutant

20 concentration in contrast to their background conditions.

Besides, a large amount of NOₓ emission, especially NO emission, is beneficial to reduce the O₃ concentrations since NO consumes O₃. Background precursors (NOx/VOCs) from boundary conditions only contribute 2%–16% and 12%–24% of NO and NO₂ concentrations and raise O₃ concentration by 5%–9%. Weaker ventilation conditions lead to accumulation of NOₓ and higher NOₓ concentration, but a lower O₃ concentrations due to the stronger NO titration effect consuming O₃.

25 Furthermore, in order to reduce the reactive pollutant concentrations under the odd-even license plate policy (reduce 50% of the total vehicle emissions), vehicle VOCs emissions should be reduced by at least another 30% to effectively lower O₃, NO and NO₂ concentrations at the same time. These results indicate that the examination of the precursors (NOₓ/VOCs) from both traffic emissions and background boundaries is the key point for better understanding O₃–NOₓ–VOCs chemistry mechanisms in street canyons and providing effective guidelines for the joint prevention and control of local street air

30 pollution.

Geoscientific
Model Development
Discussions

EGU

Keyword. CFD model; O_3–NO_x–VOCs chemistry; Urban pollution; Street canyon; OpenFOAM;

1 Introduction

35　With the worldwide rapid urbanization, air pollution in cities, such as haze and photochemical smog characterized by high-levels of the particulate matter and/or surface ozone (O_3), has become one of the widely concerned environmental problems (Lu et al., 2019; Wang et al., 2020). Recently, the observational data have shown that $PM_{2.5}$, one of the major pollutants in cites, has decreased 30%–50% across China due to strict air quality control measures (Zhai et al., 2019). At the same time, 87%, 63%, 93%, 78% and 89% of the observational stations in China have shown the decreasing trend of CO, NO_2, SO_2,

40　PM_{10} and $PM_{2.5}$ in recent 5 years, respectively (Fan et al., 2020). Various data indicate that air quality in China has been significantly improved. Unlike other pollutants, however, O_3 concentrations has increased in major urban clusters of China (Lu et al., 2018). Severe O_3 pollution episodes still exist and happen frequently (Wang et al., 2017). Therefore, research on reactive pollutants such as O_3, which has adverse effect on human health (Goodman et al., 2015; Liu et al., 2018b; Sousa et al., 2013), the productivity of crop (Rai and Agrawal, 2012), building materiel (Massey, 1999) and vegetation (Yue et al.,

45　2017), is of great significance to the further improvement of air quality especially in urban area.

From the perspective of the cause of urban air pollution, traffic-related emissions are the major part of airborne pollutant sources, including the precursors of O_3, NO_x (= NO + NO_2) and volatile organic compounds (VOCs) (Degraeuwe et al., 2017; Kangasniemi et al., 2019; Keyte et al., 2016; Pu and Yang, 2014; Wild et al., 2017; Wu et al., 2020). It has been believed that the production of O_3 is from the NO_2 photolysis. Generally, in a clean atmosphere, the produced O_3 would be

50　consumed by NO titration effect. However, with the involved VOCs, NO concentrations become lower due to the consumption with RO_2 (the production of VOCs and OH, $VOCs + OH \rightarrow RO_2 + H_2O$), which weaken the NO titration effect and consequently lead to the O_3 accumulation (Seinfeld and Pandis, 2016). In China, previous studies have shown that 22%–52% of total CO, 37%–47% of total NO_x, and 24%–41% of total VOCs emissions are contributed by the vehicle emissions in urban area (Li et al., 2017; Zhang et al., 2009; Zheng et al., 2014, 2009).

55　To investigate the formation pattern and dispersion of reactive pollutants, numerical simulation has been considered as an effective method by using the air quality models. Based on length scales, the air flow and air quality modeling in cities are commonly categorized into four groups by length scales, i.e., street scale (∼100 m), neighborhood scale (∼1 km), city scale (∼10 km), and regional scale (∼100 km) (Britter and Hanna, 2003). With the complex geometric and non-uniformity in building distribution within cities, Computational Fluid Dynamics (CFD) simulation has recently gained popularity in the

60　urban climate research (Toparlar et al., 2017). Different from the typical meso-scale (~1000km) and regional-scale (~100km) air quality models, CFD has better performance in micro-scale pollutant dispersion within the urban street canyon (~100m) or urban neighborhoods (~1 km), which are restricted spaces with more complicated turbulent mixing and poorer ventilation condition than rural areas (Zhong et al., 2015). Besides the shorter physical processes in micro-scale urban models (~100m-

1km, ~10s-100s), the rather fast chemical processes of NO_2 photolysis and NO titration with the complex chain of VOCs

65   reactions also require finer resolution model (Vardoulakis et al., 2003). For instance, CFD models with fine grid (~0.1-1m) and small timestep (~0.1s) have been effectively adopted to simulate these high-resolution spatial and temporal variations in urban areas (Sanchez et al., 2016).

With the rapid growth of the high-performance computing (HPC) platforms, computational power is no longer an obstacle. CFD simulation shows the good application prospect in urban microclimate research (Fernandez et al., 2020;

70   Garcia-Gasulla et al., 2020). Many previous studies have investigated the pivotal factors that affect the reactive pollutant distribution within the street canyon by using the CFD model, such as street-building aspect ratio (He et al., 2017; Zhang et al., 2020; Zhong et al., 2015), ambient wind conditions (Kim and Baik, 2004; Kwak et al., 2013; Merah and Noureddine, 2019; Tominaga and Stathopoulos, 2010), thermal effects (Baik et al., 2007; Kwak and Baik, 2014; Park et al., 2012, 2016), emissions from vehicle (Kim et al., 2012; Kwak and Baik, 2012; Liu et al., 2018a; Zhang et al., 2019b) or the photochemical

75   reaction mechanism (Sanchez et al., 2016; Zhong et al., 2017).

Currently, most of the simulation studies have been carried out by the application of commercial CFD software. This software has rather simple operation which is effective to save time when setting up the simulation case. However, the commercial codes are usually closed source, which is a "black box" for users (Chatzimichailidis et al., 2019). In this case, the adjustment to the equations and parameters or modifications to the model is difficult for some specific simulations.

80   Therefore, an open-source CFD code for atmospheric photolysis calculation, APFoam-1.0, was developed in this study. Open Source Field Operation and Manipulation (OpenFOAM) was selected as the platform for the APFoam framework, as OpenFOAM has good performance in computing scalability and low uncertainty levels which shows good ability in large-scale CFD simulation with million-level grid number (Robertson et al., 2015). Additionally, the solvers in OpenFOAM for specific CFD problem can be developed by using the appropriate packaged functionality, which simplifies the difficulty of

85   programming. Furthermore, OpenFOAM has been also well-developed with various pre- and post-processing utilities which are convenient for data manipulation (OpenFOAM Foundation, 2018).

This paper is organized as follows: besides this Sect. 1 of introduction, Sect. 2 presents a full description of the new chemistry module and simulation solver. Model validation for the photochemical mechanism, turbulence simulation and pollutants dispersion compared with the chemical box model and several wind tunnel experiments is discussed in Sect. 3.

90   Subsequently, in Sect. 4, a series of sensitive case has been set up to investigate the contribution of the key factors on the reactive pollutants in a typical street canyon (aspect ratio, building height/street width, H/W=1). Finally, the conclusion and future research plan for the APFoam framework are summarized in Sect. 5 and Sect. 6.

2 Model description

95

2.1 General overview

APFoam framework has been developed based on OpenFOAM which is an open-source code for CFD simulation. For the numerical solution, APFoam uses finite volume method (FVM) to discretize the governing equations and adopts arbitrary three-dimensional structured or unstructured meshes. All variables of the same cell are stored at the center of the control volume (CV), and complex geometries can be easily handled with FVM (Chauchat et al., 2017). In APFoam, Laminar, Reynolds-averaged Navier–Stokes equations (RANS) and Large eddy simulation (LES) method are available for turbulence solution. Additionally, APFoam also has complete boundary conditions to choose for numerical simulation.

Based on the OpenFOAM, APFoam has been developed to conduct the photochemical simulation within the atmosphere. Different from the general chemical reaction type, there are some new types of the gaseous reactions describing the photochemical processing. More details will be introduced in Sect. 2.2.

To make it easier to get started with APFoam, the structure of the simulation case folder is consistent with the OpenFOAM. Figure 1 shows the flow diagram of simulation set-up in APFoam. The solver of APFoam, APChemFoam for one-dimension (1D) chemistry solving is modified from the solver ChemFoam which will be introduced in detail in Sect. 2.3. Other three-dimension (3D) solvers are modified from the solver reactingFoam, including APreactingFoam for online solving coupled with flow and chemical reaction, APonlyChemReactingFoam for solving only chemical reaction with a certain flow field and APsteadyReactingFoam for online solving coupled with flow and chemical reaction in steady-state. More details will be presented in Sect. 2.4.

For the simulation running (see Figure 1), mesh files, configure files and initial condition files should be prepared before the simulation. Mesh files can be made by various ways, such as blockMesh application executable by using data from blockMeshDict or fluentMeshToFoam by converting the .msh file to OpenFOAM format. For APFoam simulation, all required configure files are also listed in Figure 1. Besides, user-defined function can be loaded at run-time without recompiling the program, via writing related configuration files in the system folder. As for initial conditions, the initial state of turbulence, environment (e.g. temperature, pressure) and chemical species are necessary for the simulation. The results of APFoam would contain the wind flow and pollutant concentrations, which can be processed by the Paraview in OpenFOAM or any other CFD post-processing tools.

2.2 Chemistry module

For photochemical calculation, there are five types of reactions in the mechanism. In the original version of OpenFOAM, these types of reactions are not included and should be added to the chemistry module prior to simulation. These types of the reactions are described as followed:

(1) Arrhenius reactions:
Arrhenius reaction is the basic reaction in the mechanism, and the rate of the Arrhenius reaction is calculated as

$$k = A \cdot (\frac{T}{300})^B \cdot \exp\left(-\frac{E}{T}\right) \tag{1}$$

where A, B and E are the parameters of the reaction rates.

130   (2) Photolysis reactions:

Photolysis reactions are first-order reactions, and the photolysis rate is calculated as

$$k_{phot} = \int_{\lambda_1}^{\lambda_2} J(\lambda) \cdot abs(\lambda) \cdot QY(\lambda)d\lambda \tag{2}$$

where k_{phot} is the first order rate for the photolysis reaction; $J(\lambda)$, $abs(\lambda)$ and $QY(\lambda)$ are the intensity of the light source, absorption cross section and the quantum yield for the reaction at wavelength λ, respectively.

135   Actually, the photolysis rate could be calculated by other photolysis rate model such as Fast-J (Wild et al., 2000), TUV (Madronich and Flocke, 1999), or obtained from photolysis data set such as IUPAC (Atkinson et al., 2003). Since the photolysis rate does not depend on temperature, in the current version of APFoam, the reaction rates are obtained from the literature (Carter, 2010) rather than online calculation in order to improve the calculation efficiency.

  (3) Falloff reactions:

140   Rate of Falloff reactions is a function of temperature and pressure which is calculated as

$$k(T,M) = \left\{ \frac{k_0(T) \cdot [M]}{1 + \frac{k_0(T) \cdot [M]}{k_{inf}(T)}} \right\} \cdot F^z \tag{3}$$

where $z = \{1 + [\frac{\log_{10}\{\frac{k_0(T) \cdot \{M\}}{k_{inf}(T)}\}}{N}]^2\}^{-1}$; [M] is the concentration of third body, which depends on total pressure; F is broadening factors. k_0 and k_{inf} are the rates of in Arrhenius form at low-pressure limit and high-pressure limit, respectively.

  (4) "Three k" reactions:

145   The rate of "Three k" reactions depends on three reaction rates in Arrhenius form. The rate is calculated as

$$k(T,M) = k_0(T) + k_3(T) \cdot [M] \cdot \left(1 + \frac{k_3(T) \cdot [M]}{k_2(T)}\right) \tag{4}$$

where k_0, k_2 and k_3 are three reaction rates and [M] is the concentration of third body.

  (5) "Two k" reactions:

The rate of "Two k" reactions depends on two reaction rates in Arrhenius form. The rate is calculated as

150
$$k(T,M) = k_1(T) + k_2(T) \cdot [M] \tag{5}$$

where k_1 and k_2 are two reaction rates and [M] is the concentration of third body.

In the current version of the APFoam, two atmospheric photochemical mechanisms are included in the model, which was SAPRC07 (Carter, 2010) and CB05 (Yarwood et al., 2005). For SAPRC07, two versions of the chemical mechanism are available, which are CS07A and SAPRC07TB. CS07A is one of the condensed versions of the mechanism, which contains

155   52 species and 173 reactions. SAPRC07TB is a more complicated version and even contains toxics species, with 141 species and 436 reactions. As for CB05, basic version with 51 species and 156 reactions is optional in the model.

Geoscientific
Model Development
Discussions

2.3 One-dimension chemical solver (APchemFoam)

In APFoam framework, one-dimension chemistry solver (i.e. chemistry box model) called APchemFoam is included in the
160   model. This solver only concerns the chemical concentration and reaction heat variation during simulation, and calculations
are started from initial conditions within a single cell mesh. The concentration and energy equation are described as
(OpenFOAM Foundation, 2018):

$$\frac{\partial \rho Y_i}{\partial t} = w_i(Y_i, T) \tag{6}$$

$$h = u_0 + \frac{p}{\rho} + \int_0^t \frac{\dot{q}}{\rho} d\tau \tag{7}$$

165

$$p = \frac{\rho R T}{M_{ave}} \tag{8}$$

where Y_i is the species mass fraction; w_i is the reaction rate; T is the temperature; u_0 is the initial energy; p is the pressure; ρ
is the density; $\dot{q}$ is the heat from reaction; R is the gas constant and M_{ave} is the average molar weight.

2.4 Three-dimensional (3D) CFD solver with photochemical reaction

170   As mentioned above, three 3D solvers for atmospheric photochemical CFD calculation, including APreactingFoam,
APonlyChemReactingFoam and APSteadyReactingFoam, are developed in the APFoam framework.

For APreactingFoam, flow field, chemical reaction and pollutant dispersion are solved simultaneously in this solver.
Firstly, the continuity governing equation in this solver is:

$$\frac{\partial \rho}{\partial t} + \nabla \cdot (\rho U) = 0 \tag{9}$$

175   Besides, the momentum governing equation is:

$$\frac{\partial \rho U}{\partial t} + \nabla \cdot (\rho U U) - \nabla \cdot \tau = -\nabla p \tag{10}$$

Additionally, the energy governing equation is:

$$\frac{\partial \rho h}{\partial t} + \nabla \cdot (\rho U h) + \frac{\partial \rho K}{\partial t} + \nabla \cdot (\rho U K) - \nabla \cdot (\alpha_{eff} \nabla h) = \frac{\partial p}{\partial t} + \dot{q} \tag{11}$$

Where ρ is the density; U is the velocity vector; p is the pressure; τ is the viscous stress tensor; h is the specific enthalpy; K
180   is the specific kinetic energy; α_{eff} is the effective thermal diffusivity coefficient; $\dot{q}$ is the heat from reaction.

Pressure-velocity coupling schemes for solving the flow field is PIMPLE algorithm, a merged PISO–SIMPLE
algorithm in OpenFOAM toolkit. This algorithm uses the steady-state solution (SIMPLE algorithm) for the flow field within
the time step. When defined tolerance criterion is reached, this algorithm uses PISO algorithm in the outer correction loop
and moves on in time (Holzmann, 2017). The PIMPLE algorithm allows the larger Courant numbers (Co >1) so that time

185 step can be increased to reduce the computation time. Besides, the governing equation for the reactive species transportation is:

$$\frac{\partial \rho Y_i}{\partial t} = -\nabla \cdot (\rho U Y_i) + \nabla \cdot (\mu \nabla Y_i) + [\Delta Y_i]_{chem} + E_i \tag{12}$$

where Y_i is the concentration of species i; ρ is the density; U is the velocity vector; μ is the kinematic viscosity; $[\Delta Y_i]_{chem}$ is the concentration change of species i from the chemical reaction; As mentioned above, $[\Delta Y_i]_{chem}$ is calculated following the
190 equations of (6)–(8). E_i is the emission source of species i.

APonlyChemReactingFoam is only capable of solving the chemical reaction and species dispersion under a certain flow field. The purpose of developing this solver is to save the computation time and reduce repetitive simulation. In general, the atmospheric chemical reactions have negligible effect on the flow field. Therefore, when the example cases to be studied do not involve the flow field change, this solver is suitable for this kind of simulation. The governing equation for the reactive
195 species transportation is consistent with APreactingFoam (Eq. (12)).

APSteadyReactingFoam is developed for solving the chemical reaction and species dispersion under the steady-state flow field. In this solver, pressure-velocity coupling scheme switches to SIMPLE algorithm for steady-state solution. The continuity governing equation in this solver is:

$$\nabla \cdot \rho U = 0 \tag{13}$$

200 Besides, the momentum governing equation is:

$$\nabla \cdot (\rho U U) = -\nabla p + \nabla \cdot (\mu \nabla U) \tag{14}$$

Also, the energy governing equation is:

$$\nabla \cdot (\rho U h) + \nabla \cdot (\rho U K) - \nabla \cdot (\alpha_{eff} \nabla h) = \dot{q} \tag{15}$$

where ρ is the density; U is the velocity vector; p is the pressure; μ is the kinematic viscosity; h is the specific enthalpy; K is
205 the specific kinetic energy; α_{eff} is the effective thermal diffusivity coefficient; $\dot{q}$ is the heat from reaction.

As for reactive species, the governing equation for the transportation still applies Eq. (12) as well, in order to ensure the stability of chemical reaction.

3 Model validation

210 ### 3.1 Photochemical reaction mechanism

To verify the accuracy of chemical reaction solution and specie concentration calculation, APFoam results are compared with the results from SAPRC box modeling software (Carter, 2010). For the chemical mechanism, CS07A is selected for validation in this study, and simulation time is set as 24h without diurnal variation (i.e. chemical reaction rate is constant during simulation).

215   Figure 2 shows the concentrations of 52 species from two models. In general, APFoam results have a good agreement with the SAPRC box model. Except that some species have large errors when the magnitude is very small (Figure 2f–h), the simulation results for other species from two models are basically consistent.

     For further investigation, relative error (RE, %) for each specie at each time step and mean relative error (MRE, %) are calculated for the selected species with large bias. These statistics are calculated as followed:

$$RE_{i,\ t} = \frac{C_{APFoam,\ i,\ t} - C_{SAPRC,\ i,\ t}}{C_{SAPRC,\ i,\ t}} \times 100\% \tag{16}$$

$$MRE_i = \frac{\sum_{t=1}^{n} \left| \frac{C_{APFoam,\ i,\ t} - C_{SAPRC,\ i,\ t}}{C_{SAPRC,\ i,\ t}} \right|}{n} \times 100\% \tag{17}$$

where $RE_{i,\ t}$ is the relative error of specie i at time step t; $C_{APFoam,\ i,\ t}$ is the concentrations of specie i at time step t from APFoam ; $C_{SAPRC,\ i,\ t}$ is the concentrations of specie i at time step t from SAPRC box model; $MRE_{i,}$ is the mean relative

225   error of specie i and n is the total number of the time step.

     Overall, most of the $RE_{i,t}$ are less than 1%, indicating that simulation error of APFoam is less than 1% during the whole simulation period. However, there are 6 species with RE and MRE greater than 1%, which are TERP, ISOPRENE, OLE1, OLE2, IPRD and ARO2. The MRE of these 6 species are 44.0%, 40.7%, 7.74%, 38.5%, 7.71% and 1.20%, respectively. Additionally, Figure 3 shows time series of RE and concentrations for these high RE and MRE value species. In Figure 3a,

230   RE values in the early stage of simulation (t = 0–180 min) are less than 1% for these species. However, the REs of TERP, ISOPRENE and OLE2 increase dramatically after t = 180 min. The REs can even up to respective 190.4%, 297.0% and 867.4% in the following simulation. It should be noted that, at the later time, the REs of these 3 species have no values because they are consumed up during the chemical reaction and their concentrations from SARPC box model become zero. The significant increase in the RE values of OLE1 and IPRD begins at t = 1020 min, with the maximum RE values of 60.1%

235   and 60.9%, respectively. Relatively, the RE of ARO2 is smaller with the value of 5.0% only.

     Figure 3b illustrates the concentrations variation of these 6 species with worst agreement from two models. It can be found that the concentrations of these 6 species keep dropping during the whole simulation period. Combined with the result of Figure 3a, the dramatical increase of RE is due to the significant concentration decrease of these 6 species. In this study case, these 6 species are continuously consumed without complementation, which results in the concentrations of these

240   species tending to be 0. For extremely small number, the processing of different model is diverse. Thus, when the reduction of magnitude excesses 10^{-5} to 10^{-6}, the RE would become much larger between two models. In the realistic situation, the concentrations of the species would not be completely consumed up with continuous emission source and boundary conditions. Therefore, the photochemical reaction simulation results of APFoam could be reliable and the overall errors might be less than 1%.

245

3.2 Numerical settings and validation study in urban flow modelling

It is well known that large eddy simulations (LES) perform more accurately in simulating urban turbulent characteristics than the Reynolds-Averaged Navier-Stokes (RANS). However, RANS models (e.g., k-ε models) are still more widely utilized because of the disadvantages of LES, such as the much more computational time and resource requirements, the

250   difficulties in setting appropriate wall boundary conditions and defining the time-dependent domain inlet, the challenges to develop advanced sub-grid scale models. Among the RANS turbulence models (Tominaga and Stathopoulos, 2013; Yoshie et al., 2007), in contrast to the modified k-ε models (e.g. realizable and RNG k-ε models), although the standard k-ε model performs worse in predicting turbulence in the strong wind region of urban districts (e.g. separate flows near building corner), the prediction accuracy is better in simulating the low-wind-speed region (e.g. weak wind in 2D street canyon sheltered by

255   buildings at both sides). Hence, as one of the widely adopted RANS methods, the standard k-ε model is selected to solve the incompressible steady-state turbulent flows in 2D street canyon. The governing equations are as below:

$$\nabla \cdot \overline{U} = 0 \tag{18}$$

$$\nabla \cdot (\overline{U}\,\overline{U}) - \nabla \cdot ((\mu + \mu_t)\nabla\overline{U}) = -\frac{1}{\rho}\nabla\bar{p} \tag{19}$$

$$\nabla \cdot (\overline{U}\rho k) = \nabla \cdot \left(\left(\mu + \frac{\mu_t}{\sigma_k}\right)\nabla k \right) = P_k - \rho\varepsilon \tag{20}$$

260

$$\nabla \cdot (\overline{U}\rho\varepsilon) = \nabla \cdot \left(\left(\mu + \frac{\mu_t}{\sigma_\varepsilon}\right)\nabla\varepsilon \right) + C_{\varepsilon_1}\frac{\varepsilon}{k}P_k - C_{\varepsilon_2}\rho\frac{\varepsilon^2}{k} \tag{21}$$

where ρ is the density; $\overline{U}$ is the time-average velocity vector; $\bar{p}$ is the time-average pressure; μ is the kinematic viscosity; μ_t is the kinematic eddy viscosity ($\mu_t = \rho C_\mu \frac{k^2}{\varepsilon}$, $C_\mu = 0.09$); P_k is the turbulence production term ($P_k = -\rho\overline{u_i'u_j'}\frac{\partial \overline{u_j}}{\partial x_i}$); C_{ε_1}, C_{ε_2}, σ_k and σ_ε are constant as 1.44, 1.92, 1.0 and 1.3, respectively.

To further evaluate the numerical accuracy of the turbulence flow simulation, a scaled CFD case is performed under the

265   estimation of wind tunnel data. In the wind tunnel experiments (Figure 4a), 25 rows of building model in total are set along the wind direction with the working section of 11 m long, 3 m wide and 1.5 m tall. For each row, building height (H), building width (B) and street width (W) are 12 cm, 5 cm and 5 cm (i.e. aspect ratio H/W=2.4), respectively. The span-wise (or lateral) length is $L = 1.25$ m $> 10H$ which is sufficient long to ensure the 2D flow characteristics in the street canyon (Hang et al., 2020; Oke, 1988; Zhang et al., 2019a), i.e. the flow in the targeted street region is determined by the external

270   flow above it but with little impacts from the lateral boundaries. Free flow wind speed in the wind tunnel experiment is 13 m/s, corresponding to the reference Re number ($Re = \frac{U_{ref}H}{v}$) in order of 10^5.

Figure 4b and 4c show the schematic diagrams of the CFD simulation domain setting for a single full-scale street canyon simulation. H and W of the street canyon are 24 m and 10 m, with spatial scale ratio of 200:1 compared with the wind tunnel experiment. Besides, the building width B and Ly in the CFD simulation are 10 m and 3.2 m ($2H/15$),

275   respectively, assuming that only a section (*Ly*=2*H*/15) of long street canyons adopted with symmetry conditions is applied at

two lateral boundaries. The minimum grid size in this case is 0.2 m with expansion ratio of 1.2 from the wall surface toward

the surrounding, which refers to the grid independence tests from our previous research (Zhang et al., 2019a). The upstream

domain inlet profiles along Line E and comparison of profiles along Line F (Figure 4c) are measured by the Laser Doppler

Anemometry (LDA) System in wind tunnel tests. Additionally, CFD inlet profiles of stream-wise velocity (u) and turbulent

280   kinetic energy (TKE) are fitted following the profiles in experimental data (Figure 5).

All governing equations for the flow and turbulent quantities are discretized by FVM and SIMPLE scheme is used for

the pressure and velocity coupling. The under-relaxation factors for pressure term, momentum term, k and ε terms are 0.3,

0.7, 0.8 and 0.8 respectively. CFD simulations do not stop until all residuals become constant. Typical residuals at

convergence are 1×10^{-6}, 1×10^{-9} and 1×10^{-6} for *Ux*, *Uy* and *Uz*, respectively, 1×10^{-7} for continuity, 1×10^{-6} for *k*, and $1\times$

285   10^{-6} for ε.

Figure 6 shows the stream-wise velocity profiles of simulation results and experimental data along the centerline (Line

F) of the street canyon. The predicted wind profile agrees well with the wind tunnel data. One main vortex structure is

formed in the street canyon. The center of the main velocity (i.e. stream-wise velocity is 0) also matches well between

simulation and experiment.

290   Furthermore, some statistical parameters, including normalized mean square error (NMSE), fractional bias (FB) and

correlation coefficient (R) are calculated by the following equations:

$$NMSE = \frac{\sum_{i=1}^{n}(O_i - P_i)^2}{\sum_{i=1}^{n}O_iP_i} \quad (22)$$

$$FB = \frac{2(\bar{O} - \bar{P})}{\bar{O} + \bar{P}} \quad (23)$$

$$R = \frac{\sum_{i=1}^{n}[(O_i - \bar{O})(P_i - \bar{P})]}{[\sum_{i=1}^{n}(O_i - \bar{O})^2]^{0.5}[\sum_{i=1}^{n}(P_i - \bar{P})^2]^{0.5}} \quad (24)$$

295   where n is the total number of measurement points; O_i is the experimental data at measurement point i; P_i is the CFD results

at measurement point i; $\bar{O}$ is the mean value of experimental data at all points; $\bar{P}$ is the mean value of CFD results at all

points. According to the pervious works (Sanchez et al., 2016), the model acceptance criteria for urban configuration are

NMSE<1.5, −0.3<FB<0.3 and R>0.8. In this simulation case, the respective NMSE, FB and R are 0.06, -0.13 and 0.95

(Table 1), which shows the good performance of the APFoam in 2D pollutant dispersion simulation.

300

3.3 Pollutant dispersion in 2D street canyon

The pollutant dispersion accuracy in 2D street canyon is validated by wind tunnel experimental data (Meroney et al., 1996).

The wind tunnel, also the CFD domain configuration is presented in Figure 7. 28 rows of the wooden bar with 27 street

305   canyons are set from upstream toward downstream along the inflow and the street axis is perpendicular to the wind direction.
Both the height (H) and width (B) of the bar are 0.06 m and the street canyon width (W) is also 0.6 m, i.e. aspect ratio (H/W)
is 1 in this study case. A pollutant line source of ethane (C_2H_6) is set to emit the pollutant in targeted street canyon.
Following the wind tunnel configuration, there are 20 bars upstream and 8 bars downstream of the targeted street canyon.
Eight measurement points are set within the targeted street canyon, and four (P4, P5, P6, P7) of them are on the leeward side

310   and the rest of four (P11, P12, P13, P14) are on the windward side. The positions of the measurement points are
demonstrated in Figure 7. Pollutant concentrations at each measurement point are normalized with respect to that of the P7
(C_i/C_7) within the street canyon (Sanchez et al., 2016; Santiago and Martín, 2008). For CFD simulation,
APonlyChemReactingFoam solver with the standard k-ε model is applied to solve the flowing field and pollutant dispersion.
The minimum grid size in this case is 0. 5 mm with expansion ratio of 1.1 from the wall surface toward surrounding, and

315   inlet velocity is constant as 3 m/s in the simulation.

As the comparison results, Figure 8 shows the normalized concentrations between the CFD simulation and experimental data.
In general, the model slightly overestimates the C_2H_6 concentrations on windward side. However, at P4, the model
concentrations for the top of the leeward side are lower than the experimental data, and the simulation results at P5
overestimates the concentrations of pollutant. In this simulation case, the respective values of NMSE, FB and R are 0.06, -

320   0.13 and 0.95 (Table 2), which shows the good performance of the APFoam in 2D pollutant dispersion simulation.

4 Numerical results in case study

4.1 Simulation configuration and CFD setting

In this study, APFoam with CS07A photochemical mechanism is applied for street air quality simulation. As shown in

325   Figure 9a, the street aspect ratio AR (H/W) is one with building height (H=24 m), street width (W=24 m) and span-wise street
length (L=30 m). Telescoping multigrid approach is adopted in the simulation with minimum grid size of 0.2 m and
expansion ratio of 1.2 from building walls to the surrounding. The total grid number is about 87300 for the whole CFD
domain. Top and two lateral boundaries of the domain are set up as the symmetry boundary condition.

Emissions area is set up at the bottom of street canyon with the pollutant source size of 18 m (width, W_E) × 30 m (length,

330   L_E) × 0.3 m (height, H_E), representing the traffic emission near street ground, and emission data are obtained from the our
previous work (Wu et al., 2020). In this study, the emissions of NO_x, VOCs and CO are 4.37 × 10^{-8}, 2.34 × 10^{-8} and 2.03 ×
10^{-7} kg m^{-3} s^{-1}, respectively. The NO and NO_2 are separated from NO_x by the ratio of 9:1, which is similar with the previous
study (Baik et al., 2007). VOCs are speciated following SAPRC mechanism and the emission fraction of the species is obtain
from the literature (Carter, 2015).

335   Figure 9b shows the probe point locations for numerical case, where temporal variations of reactive pollutant
concentrations are monitored, which include three points at pedestrian height of z = 1 m (near street bottom, at leeward side

(LB), center (CB) and windward side (WB)) and two other probe points near street top (ST, $z = 23$ m) and street center (SC, $z = 12$ m $= 0.5H$).

Power-law velocity vertical profile is adopted for the inflow boundary condition, which is described as following:

340

$$U_{in}(z) = U_{ref} \times \left(\frac{z - H}{z_{ref}}\right)^{\alpha} \tag{25}$$

$$k_{in}(z) = (U_{in}(z) \times I_{in})^2 \tag{26}$$

$$\varepsilon_{in}(z) = \frac{C_{\mu}^{\frac{3}{4}} k(z)_{in}^{\frac{3}{2}}}{\kappa z} \tag{27}$$

Here reference velocity U_{ref} is 3 m s^{-1}; reference height z_{ref} is 24 m; turbulence intensity I_{in} is 0.1; power-law exponent α is 0.22 (He et al., 2017; Zhang et al., 2019a, 2020); Von Karman constant κ is 0.41 and C_{μ} is 0.09.

345   Besides, the initial and inlet background concentrations for O_3, NO, NO_2, VOCs and CO are 60 ppbv, 5 ppbv, 15 ppbv, 40 ppbv and 400 ppbv, respectively, which are obtained from an observation campaign (Liu et al., 2008). For meteorological conditions, the temperature is 300 K and the operating pressure is 1013.25 hPa.

In all simulation cases, steady state turbulence field is first solved in advance. The result of turbulent flow would drive the chemistry solution from $t = 0$. During $t = 0$–30 min (1800 s), the emission and chemistry solution are turned on under the

350   statistically steady turbulent flow, reaching a quasi- dynamic and photostationary steady state. Data from next 60 minutes ($t = 30$–90 min, 1800–5400 s) are used for analysis. Time step of chemistry solution is set as 0.1 s in all numerical cases.

The description of all simulation cases is listed in Table 3. To investigate the effect of chemical mechanism, background condition of the precursors (BC), emission (EMIS) and wind condition (U_{ref}) on the reactive pollutant concentrations in the street canyon, the cases of BC_zero_out, EMIS_zero_out and Uref0.5 are set up in numerical

355   simulations. In the Case_BC_zero and Case_Emis_zero, the precursors of O_3 (i.e. NO_x and VOCs) are removed from domain inlet (background boundary conditions) and pollutant source emissions, respectively, and then we compare the results with Base. In the Case_Uref50%, the U_{ref} is reduced by 50% to investigate the contribution of wind condition on the chemical reaction. However, in the Case_simple_mech, only three photochemical reactions are considered in the simulation:

360

$$NO_2 + hv \rightarrow NO + O(^3P)$$

$$O(^3P) + O_2 \rightarrow O_3 + M$$

$$O_3 + NO \rightarrow NO_2 + O_2$$
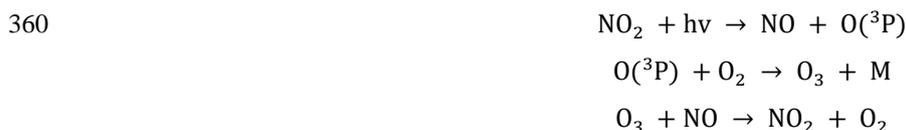
In order to improve the air quality within the urban area, some cities have tried to implement traffic control policies to reduce the pollutants from vehicle emission sources. Thus, four emission control scenarios are carried out to investigate the

365   effect of emission reduction. Case_EMIS_Ctrl50% is the scenario that reducing 50% of the traffic volume by applying such as odd-even license plate policy (i.e. reduce 50% of the total vehicle emissions). Case_EMIS_Ctrl_VOC20%, Case_EMIS_Ctrl_VOC30% and Case_EMIS_Ctrl_VOC40% are the scenarios which apply the stricter VOCs control

measures (corresponding to 20%, 30% and 40% more VOCs emission reduction, respectively) on the vehicles with traffic control policies.

370   Additionally, the change rate is used to reveal the effect of different factors on pollutant concentrations in street canyon. For each pollutant, the change rate for different cases is defined as

$$CR_p(\%) = \frac{C_{case} - C_{base}}{C_{base}} \times 100\% \quad (28)$$

where C_{case} and C_{base} are the concentrations regarded as condition change case and base case, respectively.

375 **4.2 Pollutant concentration distribution with full chemistry mechanism vs simple chemistry**

As shown in Figure 10a, one main clock-wise vortex is formed in the street canyon with AR=1. The wind speed (WS) is small near the vortex center, i.e. the minimum wind speed is approximated 0.03 m s^{-1}, which is only 1% of the speed at the domain inlet. The distributions of pollutants, such as O_3, NO and NO_2 in street canyon are also swirling (Figure 10b–d).

Leeward-side O_3 concentration in Base is less than the windward side, while NO and NO_2 are opposite. At the corner of
380   leeward side, the minimum value of O_3 and maximum value of NO_x appear, with less than 20 ppbv for O_3, more than 200 ppbv for NO and 140 ppbv for NO_2 (Figure 10b–d), respectively. Meanwhile, due to the higher NO emissions, the ratio of NO and NO_2 are higher at the bottom of the street canyon (Figure 10e). The larger NO/NO_2 values indicate that the titration effect of from NO ($O_3 + NO \rightarrow NO_2 + O_2$) and ozone depletion would be stronger, leading to the lower O_3 concentrations in this area.

385   While on the windward side, NO_x concentrations are more affected by the background conditions rather than emissions. NO_x from background conditions are less; therefore, the NO_x concentrations are lower than that on the leeward side. With the comparison of background, the windward NO and NO_2 concentrations increase approximately 35 ppbv and 55 ppbv, respectively. On one hand, pollutants from emissions are transported along the flow which increases the concentrations. On the other hand, VOCs in street canyon react with OH via the chemical reactions and generate HO_2 and RO_2. These RO_2 and
390   HO_2, O_3 would react with NO and generate NO_2, leading a higher increment for NO_2 (Figure 10f-10h). It should be noted that the O_3 concentrations could be higher due to the less depletion reaction with NO compared to that of the leeward side.

Figure 11 shows the pollutant concentrations (Figure 11a–11c) and NO to NO_2 ratio change rate of Case_simple_mech compared with the Base (Figure 11d). Without the consideration of the VOCs-related reactions in the mechanism, there is no consumption of NO by RO_2 in the mechanism (VOCs + OH → RO_2 + H_2O, RO_2 + NO → RO + NO_2), and NO titration
395   effect (O_3 + NO → NO_2 + O_2) would be stronger in this case. For the O_3, the concentrations are 36%–58% less than that in Base within the street canyon; NO_2 concentrations are also 15%–40% less and NO could be up to 91% higher than that in the simple chemistry case. Thus, the NO to NO_2 ratio would be 60%–150% higher in simple chemistry case.

4.3 Influence of background precursors of O_3 on reactive pollutant concentrations

400 In the Case_BC_zero, all background precursors of O_3 (i.e. NO_x and VOCs) from upstream domain inlet are removed. As depicted in Figure 12a, the change rates of O_3 are negative confirming that O_3 concentration becomes lower without the background NO_x and VOCs. In addition, the O_3 reduction rate on the windward side (-5% to -8%) is smaller than that on the leeward side (-9%). The influencing mechanisms of O_3 reduction are complicated and will be explained later.

On the one hand, by analyzing Figure 12b-12c, such reduction rates on the windward side for NO (-12% to -16%) and
405 NO_2 (-20% to -24%) are greater than those on the leeward side (-2% to -6% for NO and -12% to -15% for NO_2). Therefore, the ratio of NO/NO_2 increases for about 9% to 14% in the street canyon (Figure 12d). Overall, this increment of NO/NO_2 enhances O_3 depletion because the main source of ozone is the photolysis reaction of NO_2, meanwhile, the main sink is the titration effect of O_3 and NO.

On the other hand, the RO_2 from the oxidation of background VOCs with OH will consume the NO (VOCs + OH →
410 $RO_2 + H_2O$, $RO_2 + NO → RO + NO_2$), which would affect the NO_x–O_3 circulation. Figure 12e shows that the reduction of RO_2/OH on the windward side is more than that on the leeward side, which indicates that the background VOCs and OH reaction on the windward side is more active. However, due to the slower reaction rate of RO_2 and NO compared with that of HO_2 and O_3 with NO, the conversion of RO_2 to RO by reacting with NO would require more time. The reduction rate of RO/RO_2 (Figure 12f) on the leeward side (-18% to -23%) are slightly greater than that on windward side (-16% to -17%).
415 Therefore, the influence of RO_2 on NO_x–O_3 circulation would gradually appear on the leeward side, along with the flow transportation.

Additionally, Figure 12g shows the reaction rate of RO_2 $(\frac{dRO_2}{dt})$ at the bottom, center and top point on the centerline of street canyon with (base) and without (case) background conditions. At the bottom point (CB), the reduction rate of RO_2 is lower in Base. This is because the background VOCs and OH reaction consumes a portion of NO on the windward side which leads to a lower consumption of RO_2 with NO. As the simulation continues, NO concentrations would increase due to
420 the continuous release of large amounts of NO from source emissions, and the reduction rate of RO_2 become lower in Case_BC_zero due to the lack of background VOCs.

At top (ST) and center point (SC), however, as the reaction goes on and pollutants mix up, the NO concentration could become higher. Therefore, the RO_2 consumption rate is less without the background RO_2. This reduction indicates that the
425 background conditions mainly consume NO in the street canyon which leads to the increase of O_3 due to the weakening titration effect.

4.4 Effects of vehicular source emissions on reactive pollutants

430   In the Case_Emis_zero, the precursors of O_3 (NO_x and VOCs) from near-ground emissions are removed. As shown in Figure 13a, O_3 concentrations increase by over 30%-120% in the whole street canyon compare to the Base. In particular, O_3 increment on the leeward side is from 80% to 250% (not shown here) which is much higher than that on the windward side (30% to 40%). However, NO_x concentrations decrease significantly, i.e. the reduction rates are -84% to -98% for NO and -76% to -90% for NO_2, showing that the NO_x from source emissions are dominant part of NO_x in the street canyon (Figure 13b-c).

435   The large reduction of NO_x concentrations induces the increase of O_3 concentrations with weaker titration effect of O_3. Particularly, both the maximum increase for O_3 and minimum reduction of NO and NO_2 appear at the near-ground corner of the leeward side, where is the downwind area of the pollutant source. Besides, due to a larger amount of NO emissions than NO_2 (emission ratio of NO to NO_2 is 9:1), the concentration ratio of NO/NO_2 considerably decreases with the reduction rates of -30% to -70% (Figure 13d) if vehicular pollutant sources are removed.

440   Additionally, due to the large reduction of NO and NO_2 concentrations, more OH would react with VOCs instead of NO_x, which increases the RO_2 concentration (Figure 13e-13f). Meanwhile, with the reduction of NO concentration, the consumption of RO_2 significantly decreases, which leads to the dramatic increase of RO_2 concentration. Thus, the ratio of RO_2/OH rises by 115%-205% and the ration of RO/RO_2 decreases by -60% to -88%.

In Figure 13g, the reaction rate of RO_2 at three points in Case_Emis_zero is positive, which means that the RO_2 keeps
445   being generated but not consumed among these three points. Consequently, the continuous increase of RO_2 would weaken the ozone consumption. In summary, the source emissions provide a large amount of NO which enhances the O_3 depletion in the street canyon.

4.5 Influence of wind velocity reduction on reactive pollutants

450   Figure 14 shows the change rates of O_3, NO_x, and ratios when the background wind speed decreases from U_{ref} =3 m s^{-1} (Base) to U_{ref}=1.5 m s^{-1} (Case_Uref50%). In Figure 14a, there is no significant change of O_3 concentration at the center of street canyon. However, in the downwind area of the near-ground pollutant source, O_3 concentration decreases by 5% to 30%, compared with that of Base. Interestingly, at the bottom of the leeward side, O_3 has an increase up to 6% under the half inlet wind speed condition.

455   Due to the weaker capacity of pollutant dilution caused by the smaller wind speed, the concentrations of NO and NO_2 almost double (i.e. rising by 80%-98% in Figure 14b-14c) but the NO/NO_2 change rate has no significant change (-1% to -3% in Figure 14d). Besides, a higher NO_x concentration would react with more OH which consequently weakens the RO_2 production from VOCs (-8% to -20% in Figure 14e). Meanwhile, the increase of NO concentration consumes more RO_2 to RO, which leads to 180% to 340% increase of RO/RO_2 (Figure 14f).

460   Additionally, Figure 14g illustrates the RO_2 reduction in street canyon. Because of the higher concentration of NO in Case_Uref50%, the RO_2 reduction rates in three monitoring points are higher than that in Base, particularly at the bottom of

the street canyon (CB). In the early stage of the reaction, the reduction rate of RO_2 at the top point (ST) is slightly lower in Case_Uref50%. This is because that the RO_2 concentration at ST is firstly affected by the background. As the NO concentrations increases in the whole street canyon, the RO_2 consumptions become higher than that in Base.

465

4.6 Emission control strategy on reactive pollutant concentrations

Figure 15 shows the concentrations of O_3, NO and NO_2 in different NOx and VOCs emission control scenarios. In Case_Emis_ctrl50% (the emission of NO_x and VOCs reduces 50%, i.e. 50% reduction of traffic volume), the O_3

470 concentration increases from 19-47 ppbv to 29-54 ppbv (Figure 15a). On the contrary, this control measure for NO and NO_2 are very effective (Figure 15b-15c), and NO and NO_2 concentrations reduce 47% to 54% and 37% to 40% in Case_Emis_ctrl50%, respectively.

This indicates that the simple traffic control measures cannot effectively reduce O_3 concentration. It is because that most of the urban areas are the VOC-sensitive regions (Ye et al., 2016). When the total number of vehicles decreases under

475 the traffic control measures, the reduction of NO_x is higher than that of the VOCs (due to the larger NO_x emission from vehicles), which leads to a higher VOCs-to-NOx ratio, consequently resulting in a higher O_3 concentration in the street canyon (Sillman and He, 2002). Thus, in order to reduce the concentrations of O_3, the stricter VOCs control measures on vehicle should be conducted. Based on the results shown from three other emission control scenarios (Case_Emis_ctrl_VOCs20%, Case_Emis_ctrl_VOCs30% and Case_Emis_ctrl_VOCs40%) in Figure 15a, the emission of

480 VOCs needs be reduced by another 30% under traffic control (Case_Emis_ctrl50%) to bring the O_3 concentrations back to the level when no traffic control measures have been taken (Base).

As for NO and NO_2, when the additional VOCs control measures are carried on, the concentrations are higher than those in Case_Emis_ctrl50%. Even so, their concentrations do not still exceed the concentration level before the traffic control (Base), which means that such emission control scenario is still effective for the NO and NO_2. In Summary, the

485 control polies of reactive pollutants require the comprehensive consideration of the relationship between precursors and pollutants, so that the purpose to improve air quality can be achieved.

5 Conclusions

A detailed description of the Atmospheric Photolysis calculation framework APFoam-1.0 is presented in this paper, and this

490 CFD model is coupled with multiple full atmospheric photochemical mechanisms, including SAPRC07 and CB05. In order to simulate the photochemical process of reactive pollutants, five new types of the reactions, including the new form of the (1) Arrhenius reactions; (2) Photolysis reactions; (3) Falloff reactions; (4) "Three k" reactions; and (5) "Two k" reactions

have been modified and added into the APFoam. Additionally, to verify the model performance, several validations, including photochemical mechanism, flow field, 2D and 3D pollutant dispersion have been conducted in this study. The

495 model results show a good agreement with the wind tunnel experimental data, indicating that the APFoam can be applied in the analysis of micro-scale urban pollutant dispersion.

By applying the APFoam in the simulation of street canyon reactive pollutants, key factors of chemical processes are investigated. In the comparison of chemical mechanism, O_3 and NO_2 are underestimated by 36%–58% and 15%–40%, respectively, while NO is overestimated by 30%–90% without the consideration of the VOCs reactions. Other numerical

500 sensitivity cases reveal that vehicle emission is the main source of the NO and NO_2, with the contribution of 82%–98% and 75%–90%, respectively. The resident part of the NO_x in street canyon is contributed by the background concentration. However, vehicle emissions with a large amount of emitted NO_x, especially NO, is a main reason for the decrease of O_3 due to the stronger NO titration effect within the street canyon. In contrast, 5%–9% of the O_3 are contributed by the boundary conditions. Ventilation condition is another reason for the NO_x concentrations increment, and the increase of NO_x can be up

505 to 98%. However, at the downwind of the emissions, O_3 is reduced due to the increase of NO concentrations. In order to control and improve the air quality in the street canyon, traffic control policies are effective for NO_x. However, our results indicate that at least another 30% reduction in vehicle VOCs emissions can reduce the O_3 concentrations under the odd-even license plate policy. Overall, APFoam-1.0, a fully coupled CFD model, can be employed to investigate the atmospheric photolysis calculation in urban areas, and provide reliable and useful suggestions for the improvement of urban air quality.

510

6 Future plans

However, in the current version of the APFoam, aerosol chemistry is not included in the model, and it is necessary to couple with the aerosol processes, such as MOSAIC (Zaveri et al., 2008) or ISORROPIA (Fountoukis and Nenes, 2007; Nenes et al., 1998) in the future work. Besides, the photolysis rates in the current model have been fixed without the diurnal variation,

515 which means that the model is not suitable for a long-term simulation, and needs to be updated in the subsequent versions.

Code availability. The source code of the APFoam-1.0 model and examples are available on GitHub (https://github.com/vnuni23/APFoam, last access: 18 November 2020) and Zenodo

520 (https://doi.org/10.5281/zenodo.4279172). More information and help are also available by contacting the authors.

Author contributions. LW and XW designed the experiments. LW and CG developed the model code. LW and JH performed the simulations and organized the results of model cases. LW and JH prepared the article with contributions from all coauthors. XW and MS proposed revision suggestions for the article.

References

Atkinson, R., Baulch, D. L., Cox, R. A., Crowley, J. N., Hampson, R. F., Hynes, R. G., Jenkin, M. E., Rossi, M. J. and Troe, J.: Evaluated kinetic and photochemical data for atmospheric chemistry: Part 1 – gas phase reactions of O_x, HO_x, NO_x and SO_x species, Atmos. Chem. Phys. Discuss., 3(6), 6179–6699, doi:10.5194/acpd-3-6179-2003, 2003.

540   Baik, J. J., Kang, Y. S. and Kim, J. J.: Modeling reactive pollutant dispersion in an urban street canyon, Atmos. Environ., 41(5), 934–949, doi:10.1016/j.atmosenv.2006.09.018, 2007.

Britter, R. E. and Hanna, S. R.: Flow and dispersion in urban areas, Annu. Rev. Fluid Mech., 35(1), 469–496, doi:10.1146/annurev.fluid.35.101101.161147, 2003.

Carter, W. P. L.: Development of the SAPRC-07 chemical mechanism, Atmos. Environ., 44(40), 5324–5335,
545   doi:10.1016/j.atmosenv.2010.01.026, 2010.

Carter, W. P. L.: Development of a database for chemical mechanism assignments for volatile organic emissions, J. Air Waste Manag. Assoc., 65(10), 1171–1184, doi:10.1080/10962247.2015.1013646, 2015.

Chatzimichailidis, A. E., Argyropoulos, C. D., Assael, M. J. and Kakosimos, K. E.: Qualitative and quantitative investigation of multiple large eddy simulation aspects for pollutant dispersion in street canyons using OpenFOAM, Atmosphere
550   (Basel)., 10(1), doi:10.3390/atmos10010017, 2019.

Chauchat, J., Cheng, Z., Nagel, T., Bonamy, C. and Hsu, T. J.: SedFoam-2.0: A 3-D two-phase flow numerical model for sediment transport, Geosci. Model Dev., 10(12), 4367–4392, doi:10.5194/gmd-10-4367-2017, 2017.

Degraeuwe, B., Thunis, P., Clappier, A., Weiss, M., Lefebvre, W., Janssen, S. and Vranckx, S.: Impact of passenger car NOX emissions on urban NO2 pollution – Scenario analysis for 8 European cities, Atmos. Environ., 171(2), 330–337,
555   doi:10.1016/j.atmosenv.2017.10.040, 2017.

Fan, H., Zhao, C. and Yang, Y.: A comprehensive analysis of the spatio-temporal variation of urban air pollution in China during 2014–2018, Atmos. Environ., 220(April 2019), 117066, doi:10.1016/j.atmosenv.2019.117066, 2020.

Fernandez, G., Mendina, M. and Usera, G.: Heterogeneous computing (CPU-GPU) for pollution dispersion in an Urban environment, Computation, 8(1), doi:10.3390/computation8010003, 2020.

560   Fountoukis, C. and Nenes, A.: ISORROPIAII: A computationally efficient thermodynamic equilibrium model for K+-Ca2+-Mg2+-NH4+-Na+-SO42--NO3--Cl--H2O aerosols, Atmos. Chem. Phys., 7(17), 4639–4659, doi:10.5194/acp-7-4639-2007, 2007.

Garcia-Gasulla, M., Banchelli, F., Peiro, K., Ramirez-Gargallo, G., Houzeaux, G., Ben Hassan Saïdi, I., Tenaud, C., Spisso, I. and Mantovani, F.: A Generic Performance Analysis Technique Applied to Different CFD Methods for HPC, Int. J.
565   Comut. Fluid Dyn., 1–21, doi:10.1080/10618562.2020.1778168, 2020.

Goodman, J. E., Prueitt, R. L., Sax, S. N., Pizzurro, D. M., Lynch, H. N., Zu, K. and Venditti, F. J.: Ozone exposure and systemic biomarkers: Evaluation of evidence for adverse cardiovascular health impacts, Crit. Rev. Toxicol., 45(5), 412–452, doi:10.3109/10408444.2015.1031371, 2015.

Hang, J., Chen, X., Chen, G., Chen, T., Lin, Y., Luo, Z., Zhang, X. and Wang, Q.: The influence of aspect ratios and wall
570   heating conditions on flow and passive pollutant exposure in 2D typical street canyons, Build. Environ., 168, 106536, doi:10.1016/j.buildenv.2019.106536, 2020.

He, L., Hang, J., Wang, X., Lin, B., Li, X. and Lan, G.: Numerical investigations of flow and passive pollutant exposure in high-rise deep street canyons with various street aspect ratios and viaduct settings, Sci. Total Environ., 584–585, 189–206, doi:10.1016/j.scitotenv.2017.01.138, 2017.

575   Holzmann, T.: Mathematics, Numerics, Derivations and OpenFOAM., 2017.

Kangasniemi, O., Kuuluvainen, H., Heikkilä, J., Pirjola, L., Niemi, J. V., Timonen, H., Saarikoski, S., Rönkkö, T. and Maso, M. D.: Dispersion of a traffic related nanocluster aerosol near a major road, Atmosphere (Basel)., 10(6), 1–19, doi:10.3390/atmos10060309, 2019.

Keyte, I. J., Albinet, A. and Harrison, R. M.: On-road traffic emissions of polycyclic aromatic hydrocarbons and their oxy-
580   and nitro- derivative compounds measured in road tunnel environments, Sci. Total Environ., 566–567, 1131–1142, doi:10.1016/j.scitotenv.2016.05.152, 2016.

Kim, J. J. and Baik, J. J.: A numerical study of the effects of ambient wind direction on flow and dispersion in urban street canyons using the RNG k-ε turbulence model, Atmos. Environ., 38(19), 3039–3048, doi:10.1016/j.atmosenv.2004.02.047, 2004.

585   Kim, M. J., Park, R. J. and Kim, J. J.: Urban air quality modeling with full O3-NOx-VOC chemistry: Implications for O3and PM air quality in a street canyon, Atmos. Environ., 47(2), 330–340, doi:10.1016/j.atmosenv.2011.10.059, 2012.

Kwak, K. H. and Baik, J. J.: A CFD modeling study of the impacts of NO x and VOC emissions on reactive pollutant dispersion in and above a street canyon, Atmos. Environ., 46(x), 71–80, doi:10.1016/j.atmosenv.2011.10.024, 2012.

Kwak, K. H. and Baik, J. J.: Diurnal variation of NOx and ozone exchange between a street canyon and the overlying air,
590   Atmos. Environ., 86(x), 120–128, doi:10.1016/j.atmosenv.2013.12.029, 2014.

Kwak, K. H., Baik, J. J. and Lee, K. Y.: Dispersion and photochemical evolution of reactive pollutants in street canyons,
         Atmos. Environ., 70, 98–107, doi:10.1016/j.atmosenv.2013.01.010, 2013.

Li, M., Zhang, Q., Kurokawa, J. I., Woo, J. H., He, K., Lu, Z., Ohara, T., Song, Y., Streets, D. G., Carmichael, G. R., Cheng,
         Y., Hong, C., Huo, H., Jiang, X., Kang, S., Liu, F., Su, H. and Zheng, B.: MIX: A mosaic Asian anthropogenic emission
595   inventory under the international collaboration framework of the MICS-Asia and HTAP, Atmos. Chem. Phys., 17(2),
         935–963, doi:10.5194/acp-17-935-2017, 2017.

Liu, C. W., Mei, S. J. and Zhao, F. Y.: A CFD modelling study of reactive pollutant dispersion in an urban street canyon,
         IOP Conf. Ser. Earth Environ. Sci., 188(1), doi:10.1088/1755-1315/188/1/012051, 2018a.

Liu, H., Liu, S., Xue, B., Lv, Z., Meng, Z., Yang, X., Xue, T., Yu, Q. and He, K.: Ground-level ozone pollution and its
600   health impacts in China, Atmos. Environ., 173(November 2017), 223–230, doi:10.1016/j.atmosenv.2017.11.014, 2018b.

Liu, Y., Shao, M., Lu, S., Chang, C. C., Wang, J. L. and Chen, G.: Volatile Organic Compound (VOC) measurements in the
         Pearl River Delta (PRD) region, China, Atmos. Chem. Phys., 8(6), 1531–1545, doi:10.5194/acp-8-1531-2008, 2008.

Lu, H., Lyu, X., Cheng, H., Ling, Z. and Guo, H.: Overview on the spatial-temporal characteristics of the ozone formation
         regime in China, Environ. Sci. Process. Impacts, 21(6), 916–929, doi:10.1039/c9em00098d, 2019.

605 Lu, X., Hong, J., Zhang, L., Cooper, O. R., Schultz, M. G., Xu, X., Wang, T., Gao, M., Zhao, Y. and Zhang, Y.: Severe
         Surface Ozone Pollution in China: A Global Perspective, Environ. Sci. Technol. Lett., 5(8), 487–494,
         doi:10.1021/acs.estlett.8b00366, 2018.

Madronich, S. and Flocke, S.: The Role of Solar Radiation in Atmospheric Chemistry, pp. 1–26., 1999.

Massey, S. W.: The effects of ozone and NO(x) on the deterioration of calcareous stone, Sci. Total Environ., 227(2–3), 109–
610   121, doi:10.1016/S0048-9697(98)00409-4, 1999.

Merah, A. and Noureddine, A.: Reactive pollutants dispersion modeling in a street canyon, Int. J. Appl. Mech. Eng., 24(1),
         91–103, doi:10.2478/ijame-2019-0006, 2019.

Meroney, R. N., Pavageau, M., Rafailidis, S. and Schatzmann, M.: Study of line source characteristics for 2-D physical
         modelling of pollutant dispersion in street canyons, J. Wind Eng. Ind. Aerodyn., 62(1), 37–56, doi:10.1016/S0167-
615   6105(96)00057-8, 1996.

Nenes, A., Pilinis, C. and Pandis., S. N.: ISORROPIA: A New Thermodynamic Model for Multiphase Multicomponent
         Inorganic Aerosols., Aquat. Geochemistry, 4, 123–152, 1998.

Oke, T. R.: Street design and urban canopy layer climate, Energy Build., 11(1–3), 103–113, doi:10.1016/0378-
         7788(88)90026-6, 1988.

620 OpenFOAM Foundation: OpenFoam user guide. Version 6, [online] Available from: https://openfoam.org/, 2018.

Park, S. B., Baik, J. J., Raasch, S. and Letzel, M. O.: A large-eddy simulation study of thermal effects on turbulent flow and dispersion in and above a street canyon, J. Appl. Meteorol. Climatol., 51(5), 829–841, doi:10.1175/JAMC-D-11-0180.1, 2012.

Park, S. J., Choi, W., Kim, J. J., Kim, M. J., Park, R. J., Han, K. S. and Kang, G.: Effects of building–roof cooling on the
625   flow and dispersion of reactive pollutants in an idealized urban street canyon, Build. Environ., 109(2), 175–189, doi:10.1016/j.buildenv.2016.09.011, 2016.

Pu, Y. and Yang, C.: Estimating urban roadside emissions with an atmospheric dispersion model based on in-field measurements, Environ. Pollut., 192, 300–307, doi:10.1016/j.envpol.2014.05.019, 2014.

Rai, R. and Agrawal, M.: Impact of tropospheric ozone on crop plants, Proc. Natl. Acad. Sci. India Sect. B - Biol. Sci., 82(2),
630   241–257, doi:10.1007/s40011-012-0032-2, 2012.

Robertson, E., Choudhury, V., Bhushan, S. and Walters, D. K.: Validation of OpenFOAM numerical methods and turbulence models for incompressible bluff body flows, Comput. Fluids, 123, 122–145, doi:10.1016/j.compfluid.2015.09.010, 2015.

Sanchez, B., Santiago, J. L., Martilli, A., Palacios, M. and Kirchner, F.: CFD modeling of reactive pollutant dispersion in
635   simplified urban configurations with different chemical mechanisms, Atmos. Chem. Phys., 16(18), 12143–12157, doi:10.5194/acp-16-12143-2016, 2016.

Santiago, J. L. and Martín, F.: SLP-2D: A new Lagrangian particle model to simulate pollutant dispersion in street canyons, Atmos. Environ., 42(17), 3927–3936, doi:10.1016/j.atmosenv.2007.05.038, 2008.

Seinfeld, J. H. and Pandis, S. N.: Atmospheric Chemistry and Physics: From Air Pollution to Climate Change, John Wiley &
640   Sons,Inc., 2016.

Sillman, S. and He, D.: Some theoretical results concerning O_3 -NO_x -VOC chemistry and NO_x -VOC indicators, J. Geophys. Res., 107(D22), 4659, doi:10.1029/2001JD001123, 2002.

Sousa, S. I. V., Alvim-Ferraz, M. C. M. and Martins, F. G.: Health effects of ozone focusing on childhood asthma: What is now known - a review from an epidemiological point of view, Chemosphere, 90(7), 2051–2058,
645   doi:10.1016/j.chemosphere.2012.10.063, 2013.

Tang, X., Zhang, Y. and Shao, M.: Atmospheric Environmental Chemistry, Higher Education Press, Beijing, China., 2006.

Tominaga, Y. and Stathopoulos, T.: Numerical simulation of dispersion around an isolated cubic building: Model evaluation of RANS and LES, Build. Environ., 45(10), 2231–2239, doi:10.1016/j.buildenv.2010.04.004, 2010.

Tominaga, Y. and Stathopoulos, T.: CFD simulation of near-field pollutant dispersion in the urban environment: A review of
650   current modeling techniques, Atmos. Environ., 79, 716–730, doi:10.1016/j.atmosenv.2013.07.028, 2013.

Toparlar, Y., Blocken, B., Maiheu, B. and van Heijst, G. J. F.: A review on the CFD analysis of urban microclimate, Renew. Sustain. Energy Rev., 80(January), 1613–1640, doi:10.1016/j.rser.2017.05.248, 2017.

Vardoulakis, S., Fisher, B. E. A., Pericleous, K. and Gonzalez-Flesca, N.: Modelling air quality in street canyons: A review, Atmos. Environ., 37(2), 155–182, doi:10.1016/S1352-2310(02)00857-9, 2003.

655   Wang, S., Gao, S., Li, S. and Feng, K.: Strategizing the relation between urbanization and air pollution: Empirical evidence
            from global countries, J. Clean. Prod., 243, 118615, doi:10.1016/j.jclepro.2019.118615, 2020.

        Wang, T., Xue, L., Brimblecombe, P., Lam, Y. F., Li, L. and Zhang, L.: Ozone pollution in China: A review of
            concentrations, meteorological influences, chemical precursors, and effects, Sci. Total Environ., 575, 1582–1596,
            doi:10.1016/j.scitotenv.2016.10.081, 2017.

660   Wild, O., Zhu, X. and Prather, M. J.: Fast-J: Accurate simulation of in- and below-cloud photolysis in tropospheric chemical
            models, J. Atmos. Chem., 37(3), 245–282, doi:10.1023/A:1006415919030, 2000.

        Wild, R. J., Dubé, W. P., Aikin, K. C., Eilerman, S. J., Neuman, J. A., Peischl, J., Ryerson, T. B. and Brown, S. S.: On-road
            measurements of vehicle NO2/NOx emission ratios in Denver, Colorado, USA, Atmos. Environ., 148(2), 182–189,
            doi:10.1016/j.atmosenv.2016.10.039, 2017.

665   Wu, L., Chang, M., Wang, X., Hang, J., Zhang, J., Wu, L. and Shao, M.: Development of the Real-time On-road Emission
            (ROE v1.0) model for street-scale air quality modeling based on dynamic traffic big data, Geosci. Model Dev., 13(1),
            23–40, doi:10.5194/gmd-13-23-2020, 2020.

        Yarwood, G., Rao, S., Yocke, M. and Whitten, G. Z.: Updates to the carbon bond chemical mechanism: CB05, Rep. RT-
            0400675, 246 pp.,. [online] Available from: http://www.camx.com/files/cb05_final_report_120805.aspx, 2005.

670   Ye, L., Wang, X., Fan, S., Chen, W., Chang, M., Zhou, S., Wu, Z. and Fan, Q.: Photochemical indicators of ozone sensitivity:
            application in the Pearl River Delta, China, Front. Environ. Sci. Eng., 10(6), 1–14, doi:10.1007/s11783-016-0887-1,
            2016.

        Yoshie, R., Mochida, A., Tominaga, Y., Kataoka, H., Harimoto, K., Nozu, T. and Shirasawa, T.: Cooperative project for
            CFD prediction of pedestrian wind environment in the Architectural Institute of Japan, J. Wind Eng. Ind. Aerodyn.,
675   95(9–11), 1551–1578, doi:10.1016/j.jweia.2007.02.023, 2007.

        Yue, X., Unger, N., Harper, K., Xia, X., Liao, H., Zhu, T., Xiao, J., Feng, Z. and Li, J.: Ozone and haze pollution weakens
            net primary productivity in China, Atmos. Chem. Phys., 17(9), 6073–6089, doi:10.5194/acp-17-6073-2017, 2017.

        Zaveri, R. A., Easter, R. C., Fast, J. D. and Peters, L. K.: Model for Simulating Aerosol Interactions and Chemistry
            (MOSAIC), J. Geophys. Res. Atmos., 113(13), 1–29, doi:10.1029/2007JD008782, 2008.

680   Zhai, S., Jacob, D. J., Wang, X., Shen, L., Li, K., Zhang, Y., Gui, K., Zhao, T. and Liao, H.: Fine particulate matter
            (PM<sub>2.5</sub>) trends in China, 2013&ndash;2018: contributions from meteorology, Atmos.
            Chem. Phys. Discuss., 1–19, doi:10.5194/acp-2019-279, 2019.

        Zhang, K., Chen, G., Wang, X., Liu, S., Mak, C. M., Fan, Y. and Hang, J.: Numerical evaluations of urban design technique
            to reduce vehicular personal intake fraction in deep street canyons, Sci. Total Environ., 653, 968–994,
685   doi:10.1016/j.scitotenv.2018.10.333, 2019a.

        Zhang, K., Chen, G., Zhang, Y., Liu, S., Wang, X., Wang, B. and Hang, J.: Integrated impacts of turbulent mixing and NOX-
            O3 photochemistry on reactive pollutant dispersion and intake fraction in shallow and deep street canyons, Sci. Total
            Environ., 712, 135553, doi:10.1016/j.scitotenv.2019.135553, 2020.

Zhang, Q., Streets, D. G., Carmichael, G. R., He, K. B., Huo, H., Kannari, A., Klimont, Z., Park, I. S., Reddy, S., Fu, J. S.,
690   Chen, D., Duan, L., Lei, Y., Wang, L. T. and Yao, Z. L.: Asian emissions in 2006 for the NASA INTEX-B mission,
       Atmos. Chem. Phys., 9(14), 5131–5153, doi:10.5194/acp-9-5131-2009, 2009.

Zhang, Y., Yang, X., Yang, H., Zhang, K., Wang, X., Luo, Z., Hang, J. and Zhou, S.: Numerical investigations of reactive
       pollutant dispersion and personal exposure in 3D urban-like models, Build. Environ., 106569,
       doi:10.1016/j.buildenv.2019.106569, 2019b.

695 Zheng, B., Huo, H., Zhang, Q., Yao, Z. L., Wang, X. T., Yang, X. F., Liu, H. and He, K. B.: High-resolution mapping of
       vehicle emissions in China in 2008, Atmos. Chem. Phys., 14(18), 9787–9805, doi:10.5194/acp-14-9787-2014, 2014.

Zheng, J., Che, W., Wang, X., Louie, P. and Zhong, L.: Road-network-based spatial allocation of on-road mobile source
       emissions in the pearl river delta region, China, and comparisons with population-based approach, J. Air Waste Manag.
       Assoc., 59(12), 1405–1416, doi:10.3155/1047-3289.59.12.1405, 2009.

700 Zhong, J., Cai, X. M. and Bloss, W. J.: Modelling the dispersion and transport of reactive pollutants in a deep urban street
       canyon: Using large-eddy simulation, Environ. Pollut., 200, 42–52, doi:10.1016/j.envpol.2015.02.009, 2015.

Zhong, J., Cai, X. M. and Bloss, W. J.: Large eddy simulation of reactive pollutants in a deep urban street canyon: Coupling
       dynamics with O3-NOx-VOC chemistry, Environ. Pollut., 224, 171–184, doi:10.1016/j.envpol.2017.01.076, 2017.

705
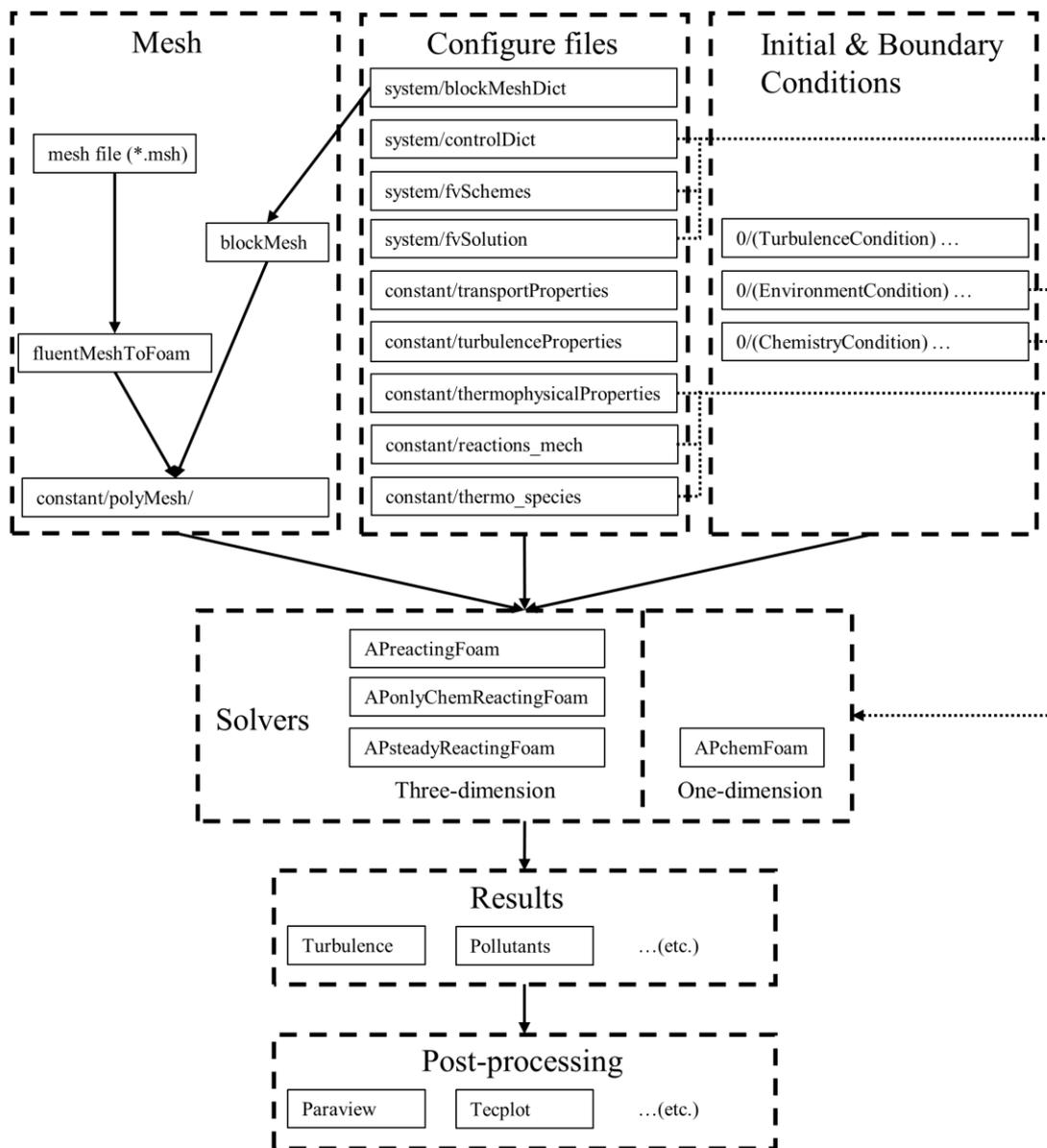
710 **Figure 1. Flow diagram of simulation set-up in APFoam framework**

(a)   (b)

(c)

(d)

(e)

(f)

(g)

(h)
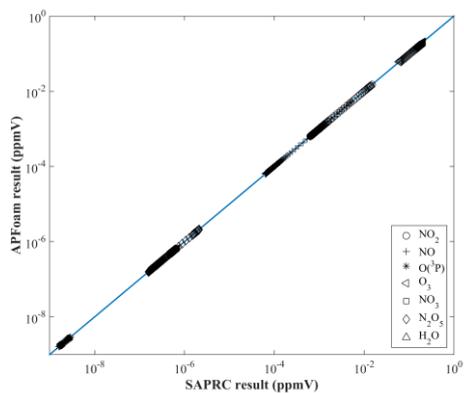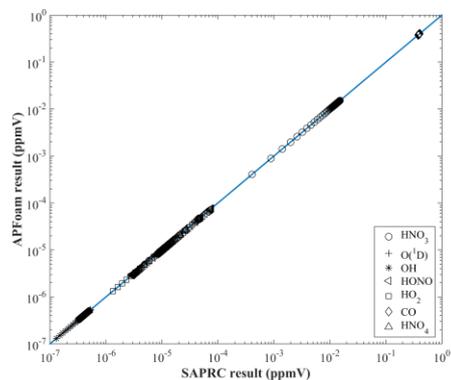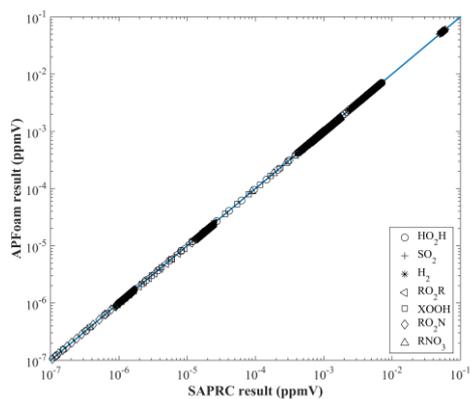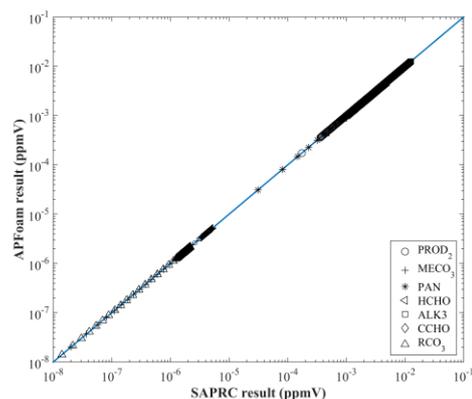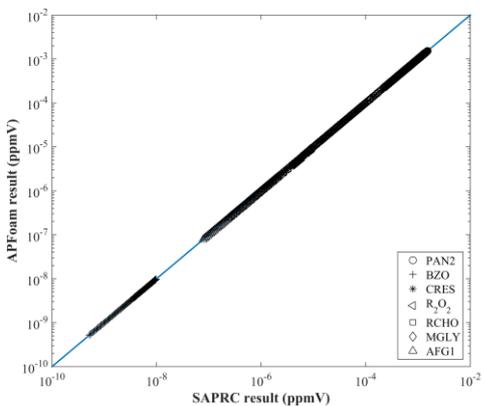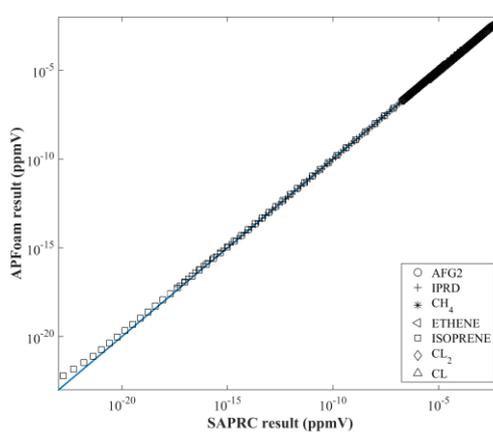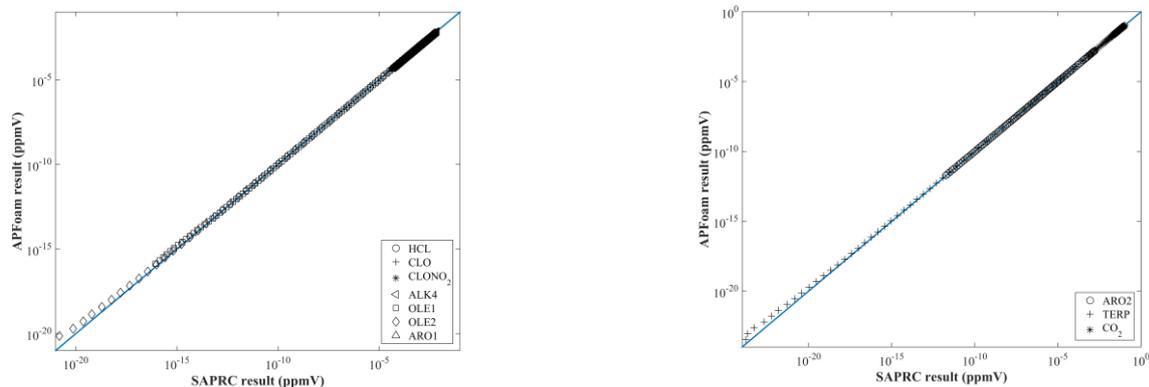
Figure 2. The comparison of concentration result between APFoam and SAPRC box model
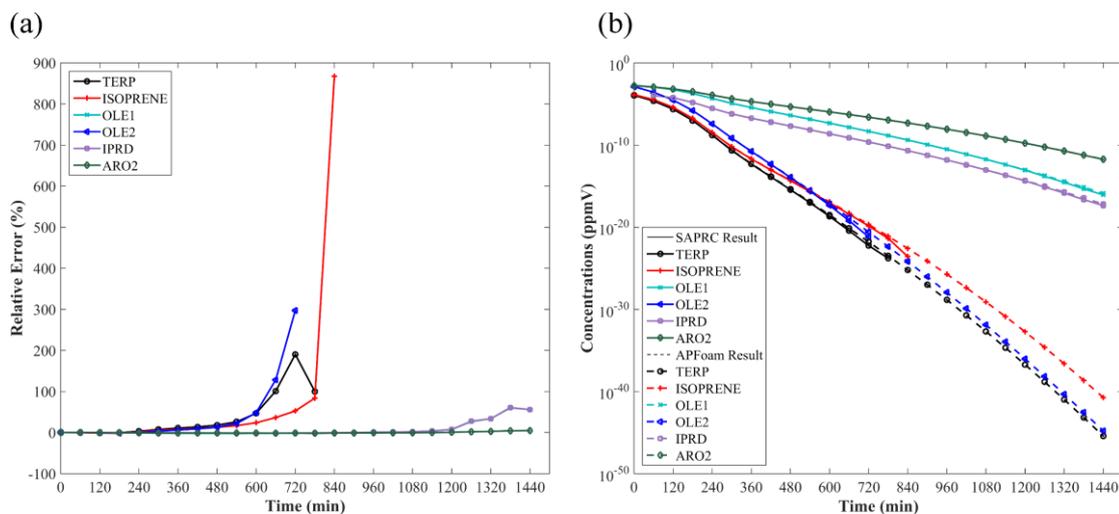
Figure 3. The time series of (a) relative error (%) and (b) concentrations (ppmv) of 6 species with largest bias

26
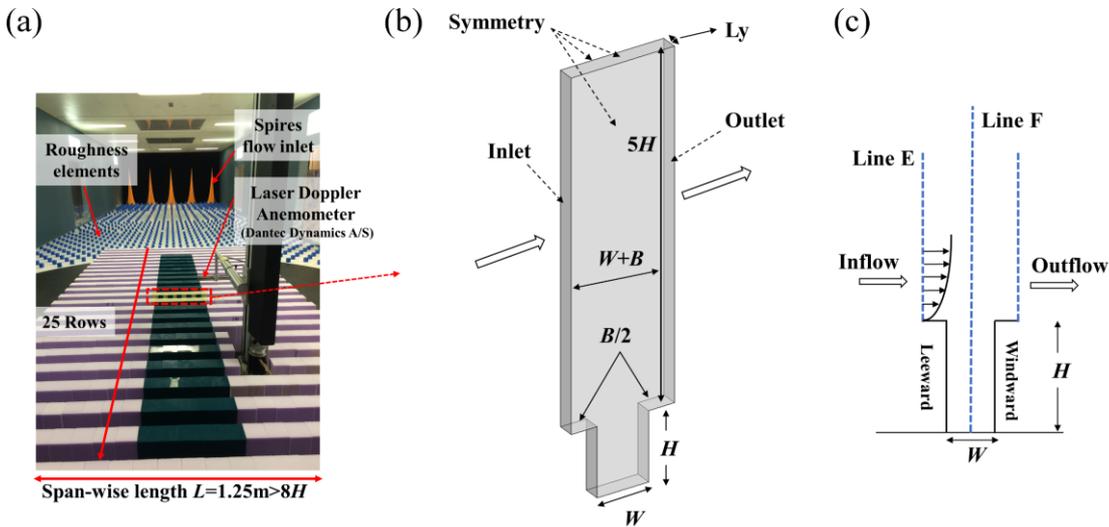
Figure 4. (a) Wind tunnel experiment in 2D street canyon; (b) the single street canyon CFD domain setups in scaled model and (c) the inlet profile (Line E) and measurement profiles (Line F) in the street canyon.
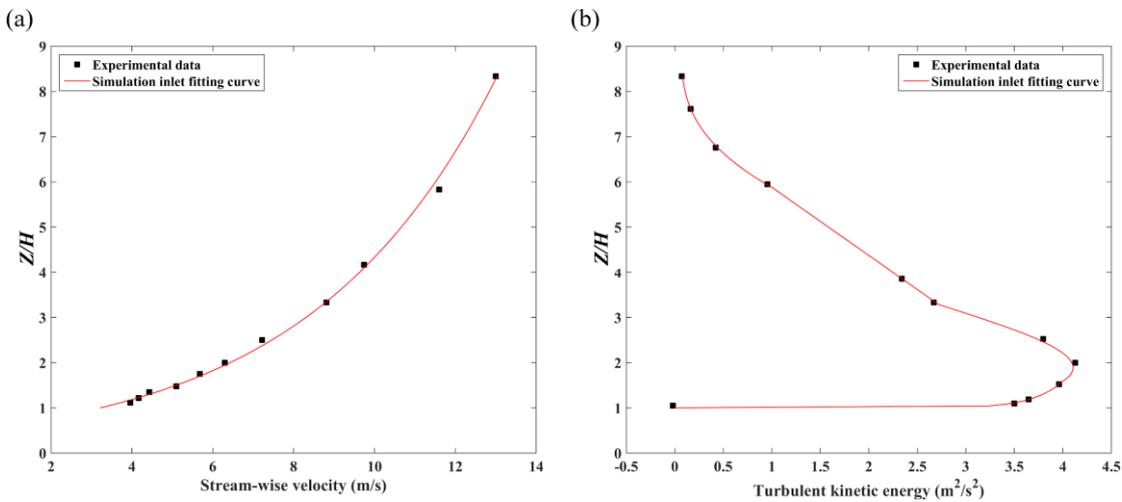
Figure 5. The inlet profile of (a) stream-wise velocity and (b) turbulent kinetic energy in single street canyon case
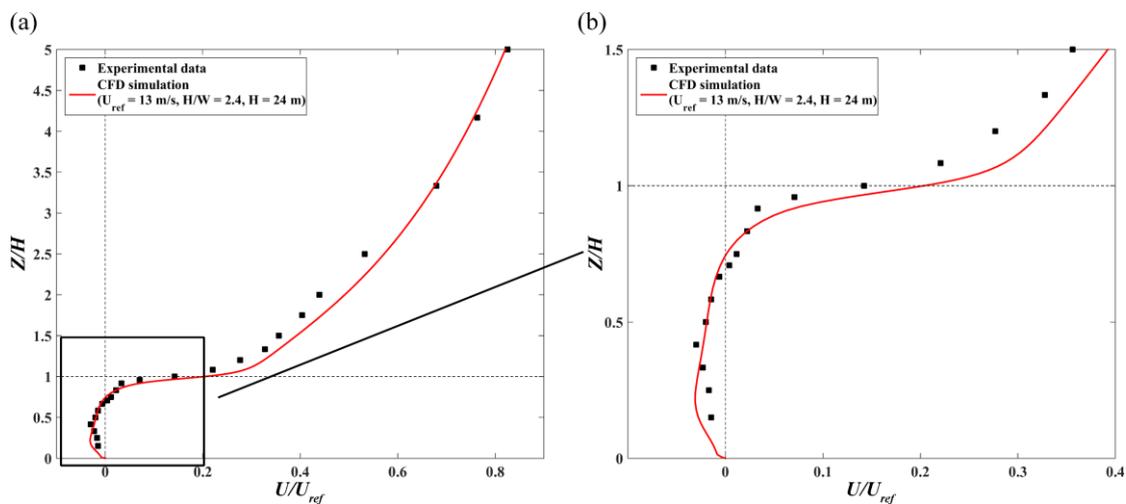
Figure 6. The stream-wise velocity profiles along the Line F

730
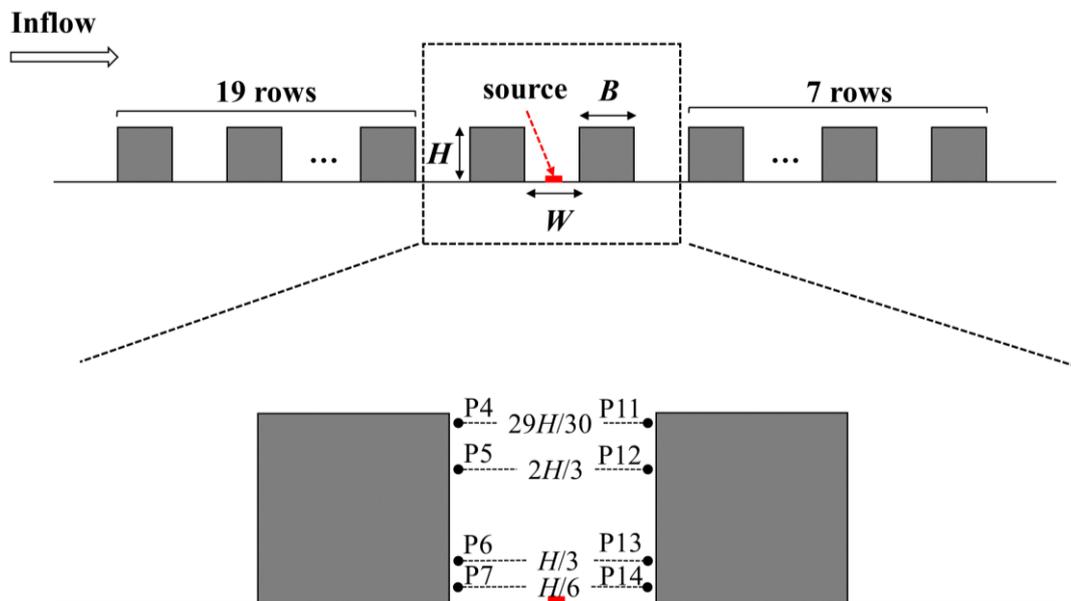
Figure 7. the schematic diagram of the 2D pollutant dispersion simulation setting
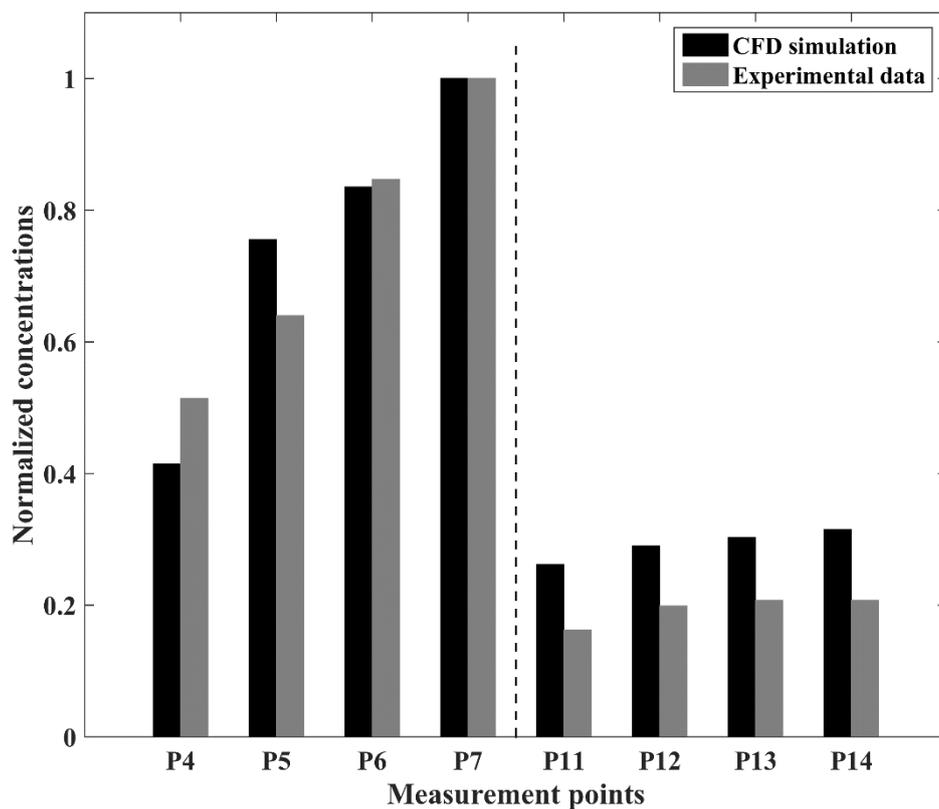
Figure 8. Normalized concentrations of CFD and experimental data at each measurement point in 2D dispersion case
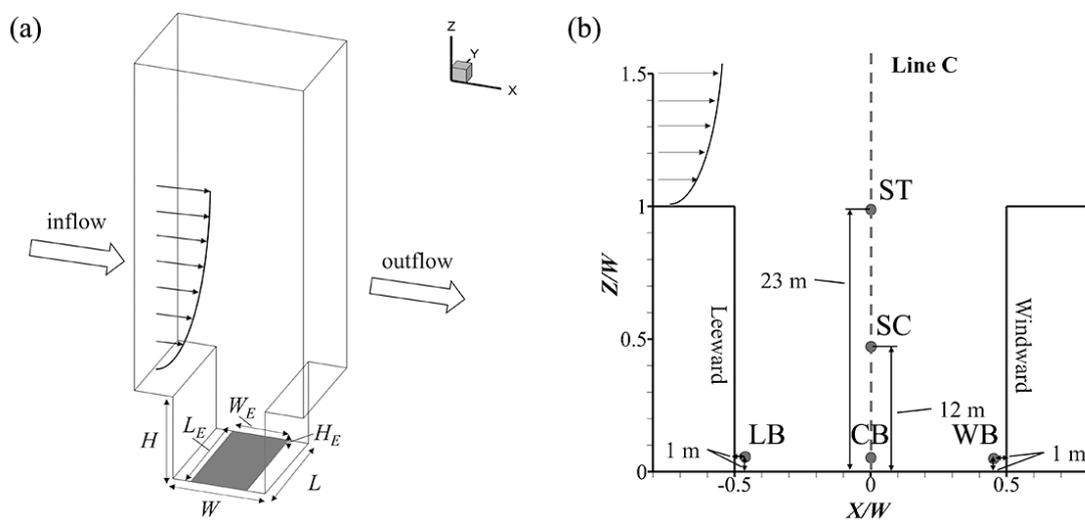
Figure 9. Schematic diagram of (a) the CFD simulation domain and (b) the probe points location

740

(a)

(b)

(c)

(d)

(e)

(f)
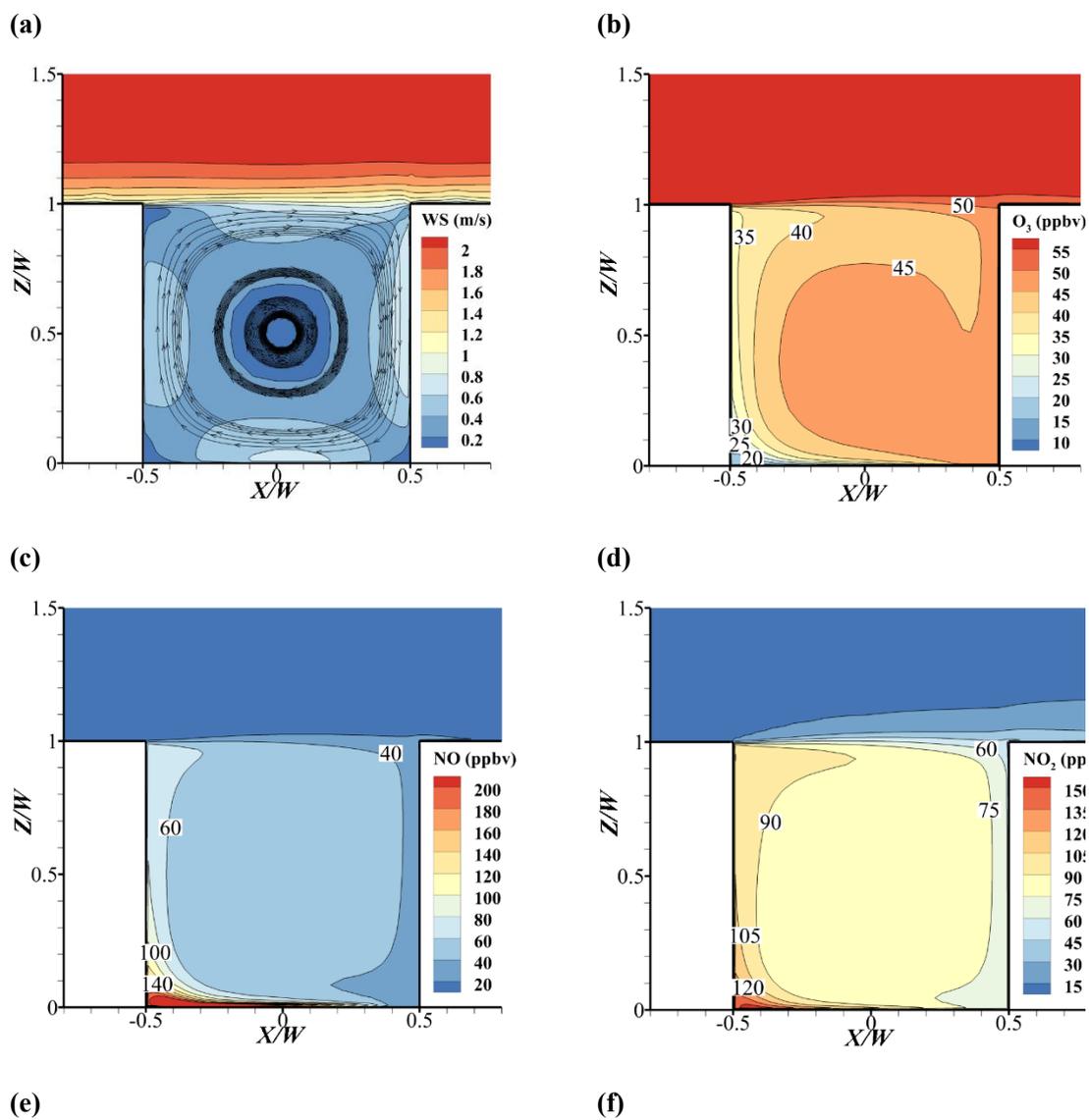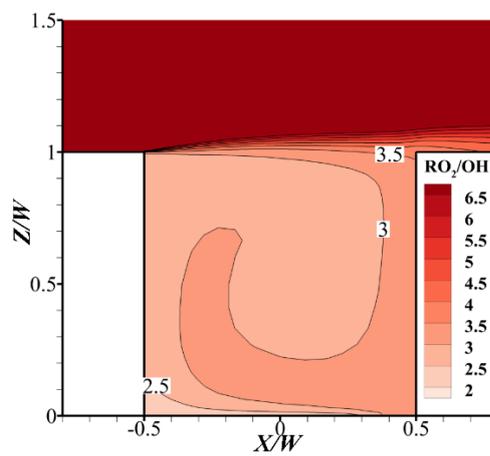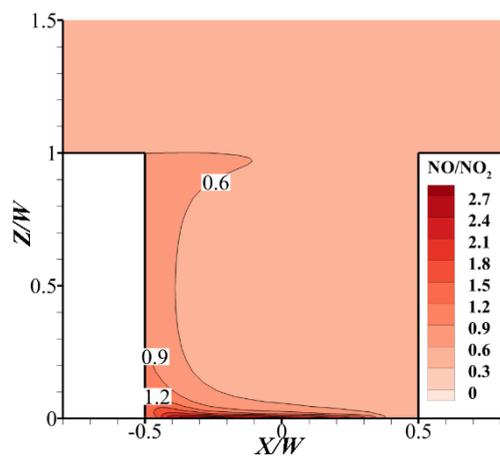
(g)

(h)
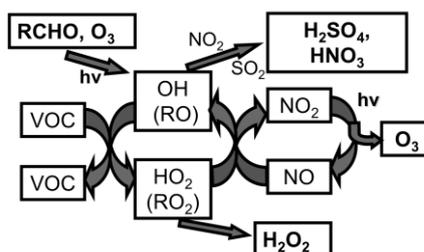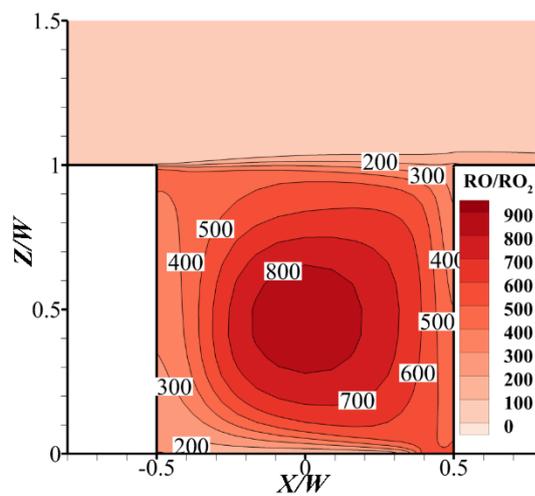
Figure 10. (a) Flow field and pollutant distribution of (b) O_3, (c) NO, (d) NO_2, (e) NO/NO_2, (f) RO_2/OH, (g) RO/RO_2 in Base and (h) Schematic diagram of the formation mechanism of photochemical reactions (Tang et al., 2006)

(a)   (b)
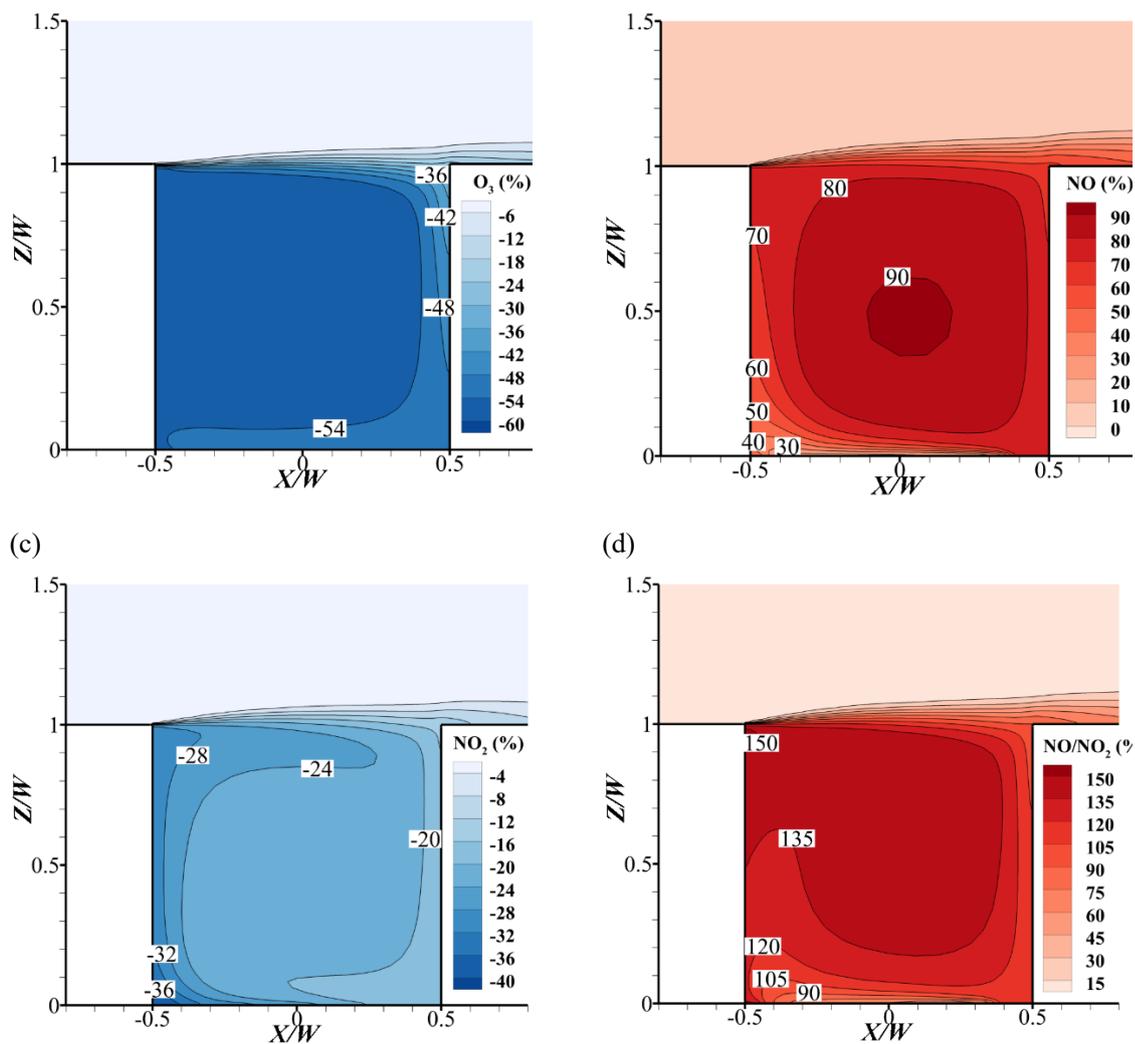
Figure 11. Change rate of (a) O₃, (b) NO, (c) NO₂, (d) NO/NO₂ between simple chemistry and full chemistry mechanism

(a)   (b)

(g)
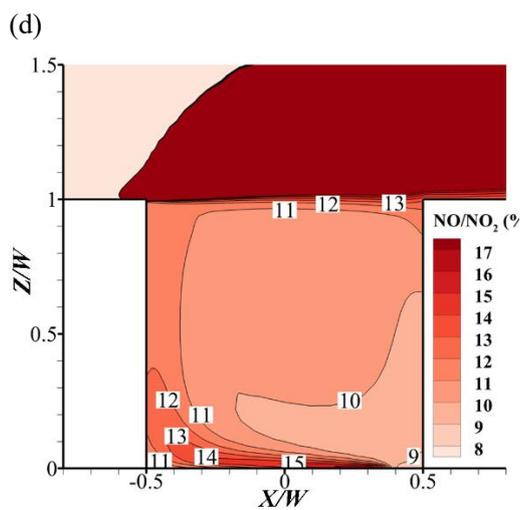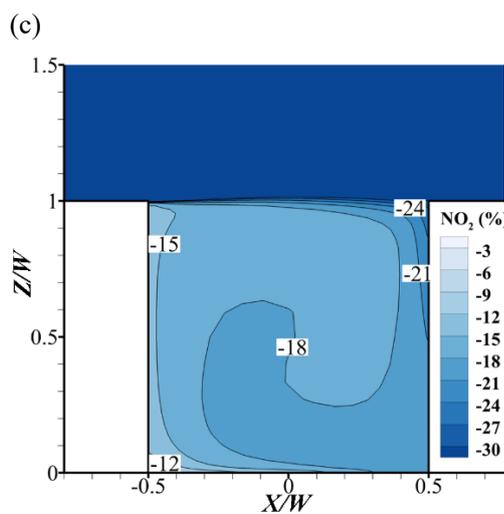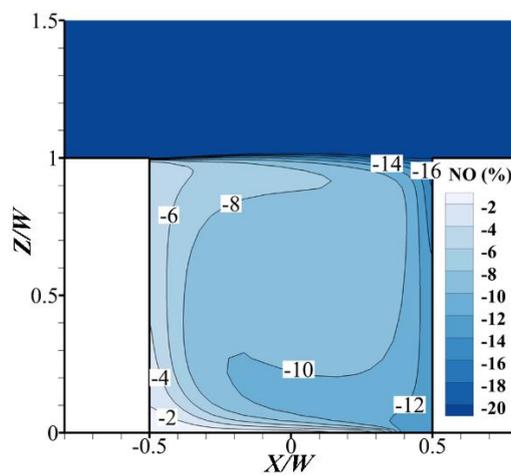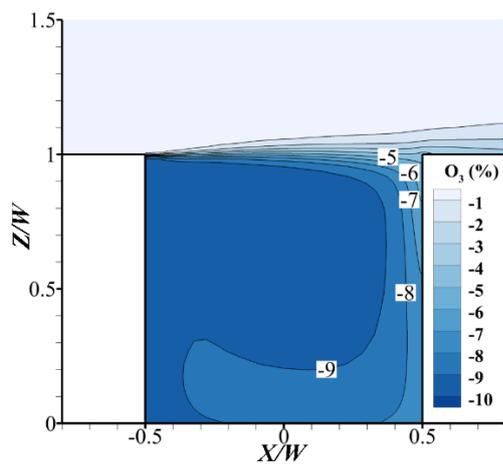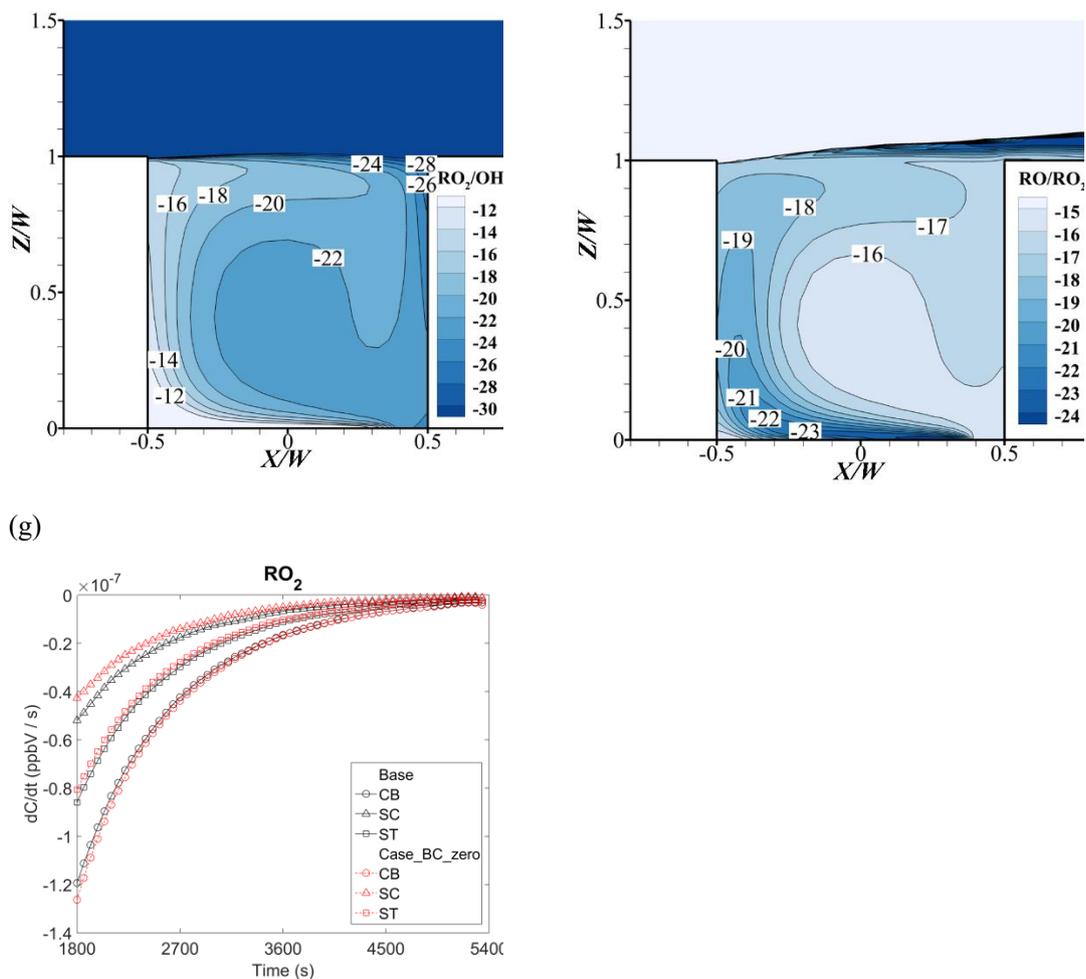
Figure 12. Change rate of (a) O_3, (b) NO, (c) NO_2, (d) NO/NO_2, (e) RO_2/OH, (f) RO/RO_2 at t = 5400 s and (g) time series of reaction rate of RO_2 ($\frac{dRO_2}{dt}$) of Case_BC_zero

750

(a)   (b)

(c)

(d)

(e)

(f)

(g)

Figure 13. Change rate of (a) O_3, (b) NO, (c) NO_2, (d) NO/NO_2, (e) RO_2/OH, (f) RO/RO_2 at t = 5400 s and (g) time series of reaction rate of RO_2 ($\frac{dRO_2}{dt}$) of Case_Emis_zero

(a)   (b)

(c)

(d)
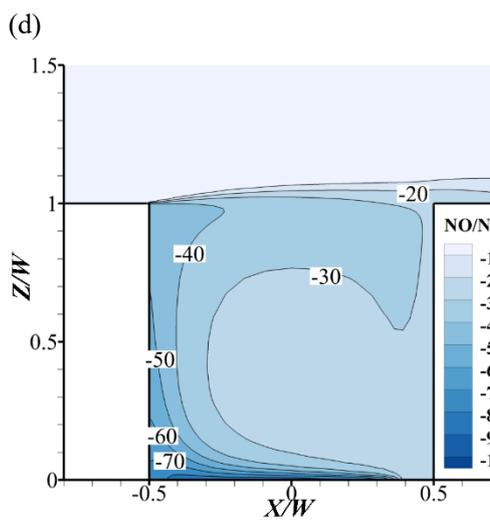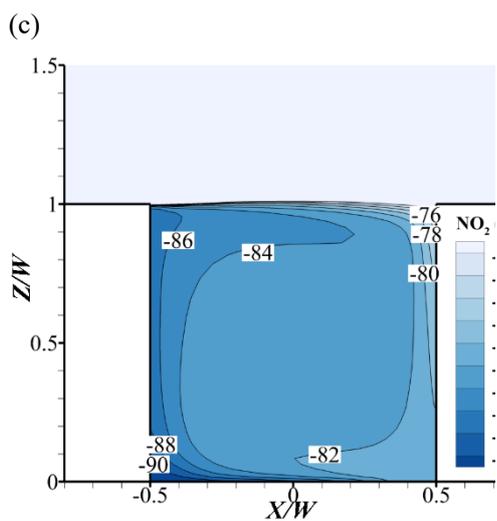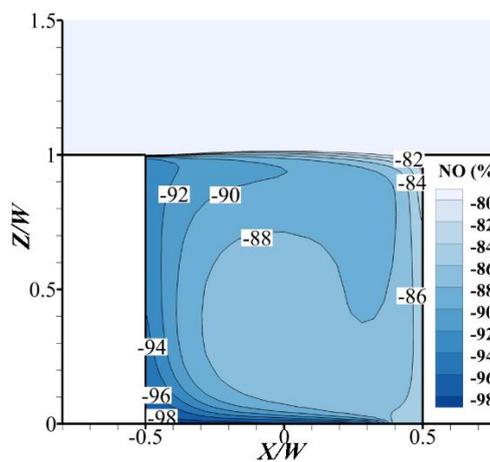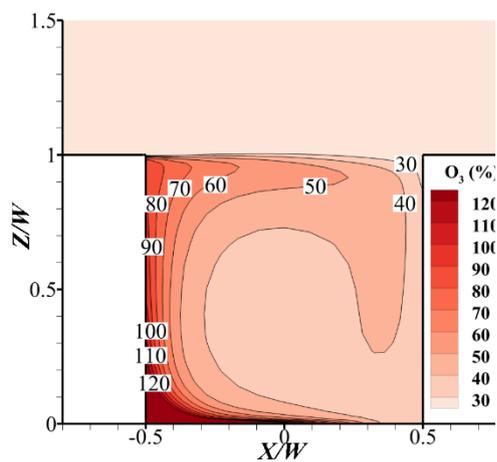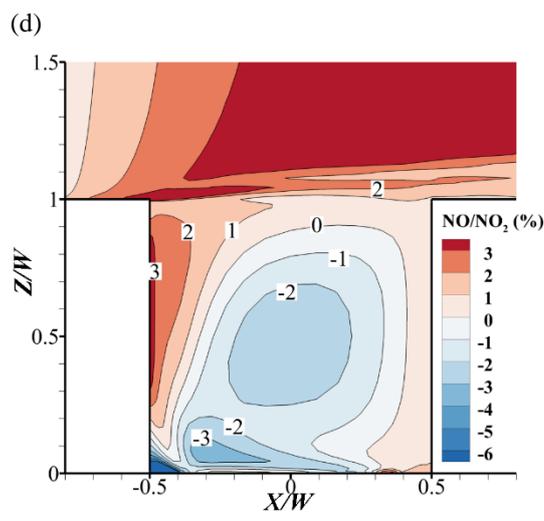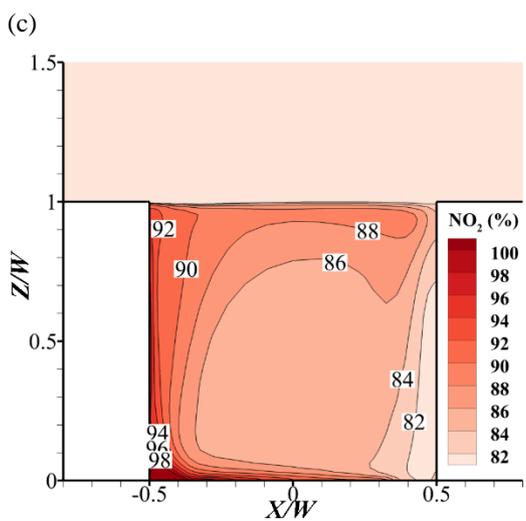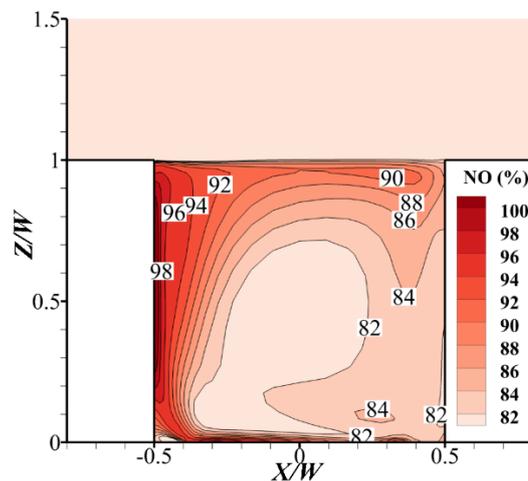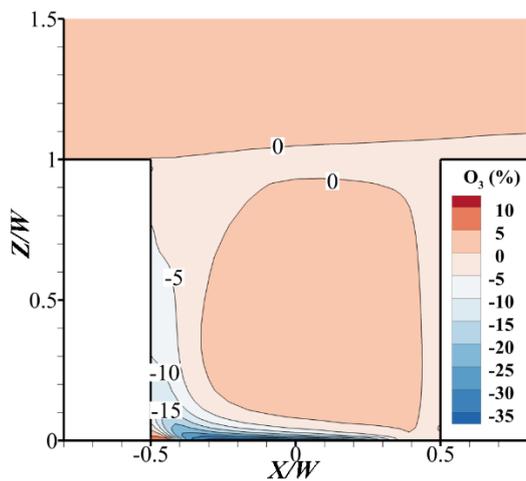
(e)

(f)
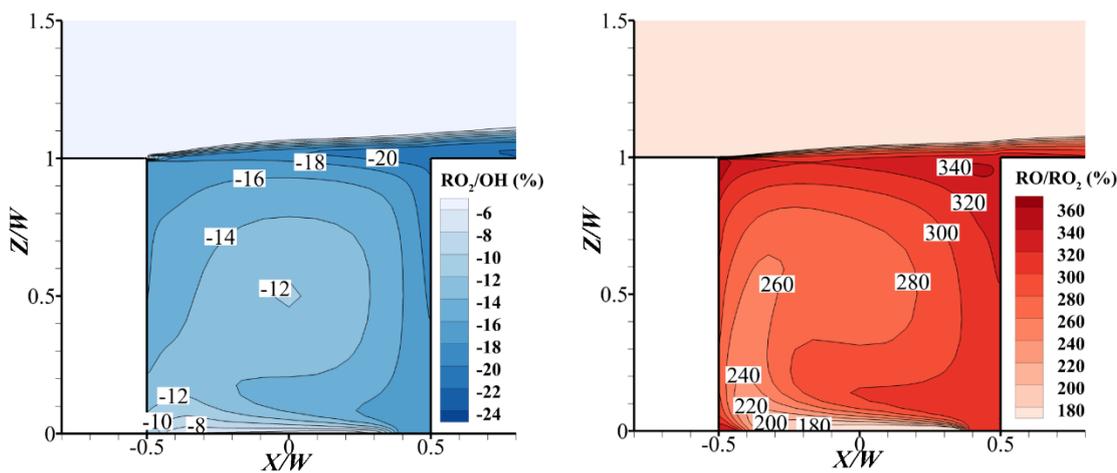
(g)
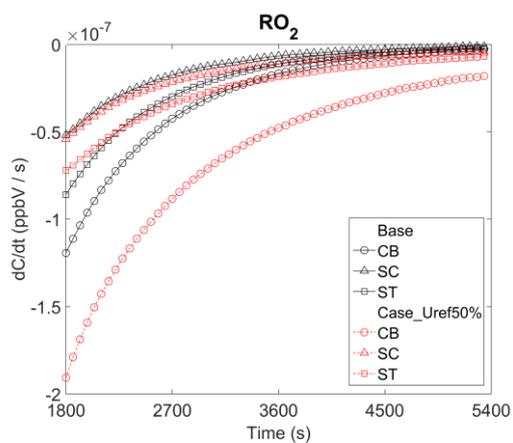
Figure 14. Change rate of (a) O_3, (b) NO, (c) NO_2, (d) NO/NO_2, (e) RO_2/OH, (f) RO/RO_2 at t = 5400 s and (g) time series of reaction rate of RO_2 ($\frac{dRO_2}{dt}$) of Case_Uref50%

(a)

(b)
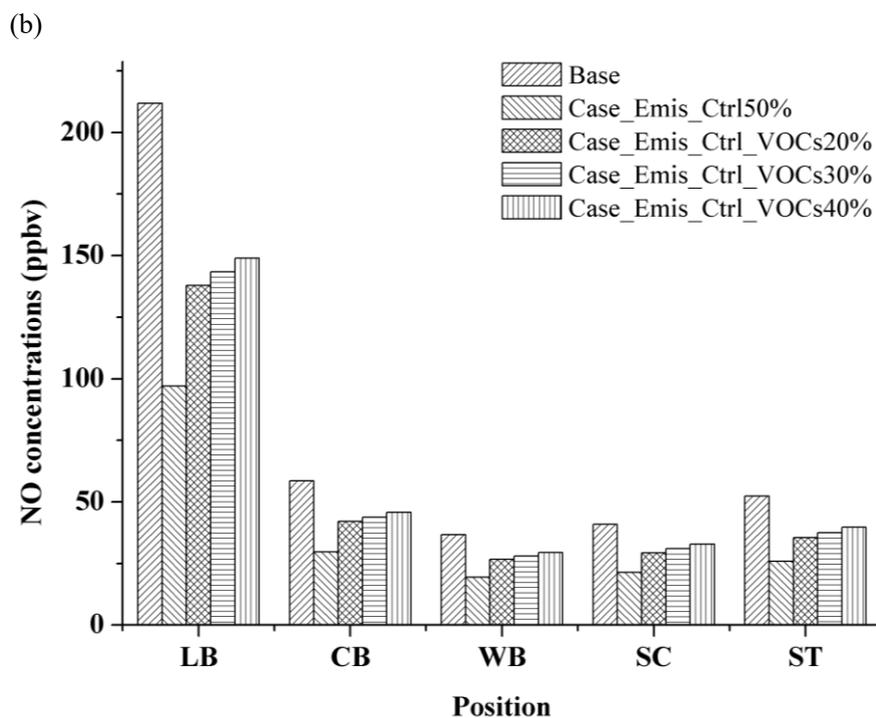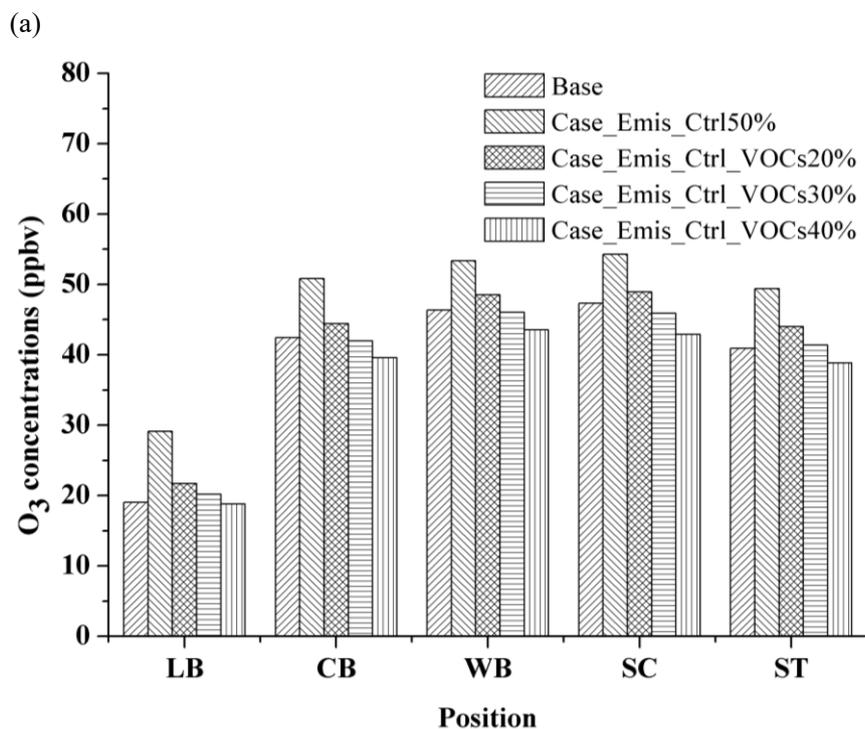
(c)
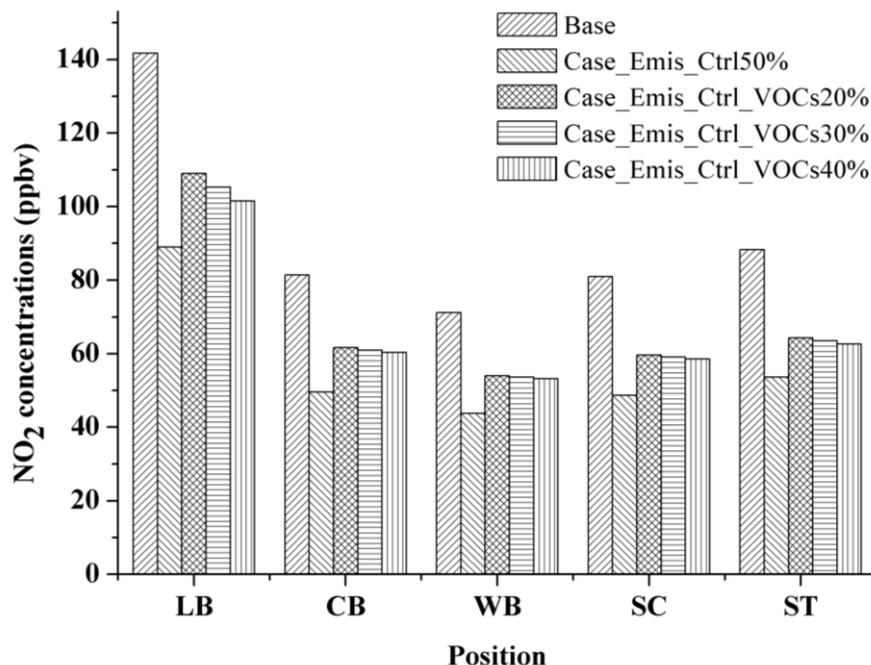
Figure 15. The (a) O₃, (b) NO and (c) NO₂ concentrations in different emission control scenarios

Table 1. Statics values of the turbulence flow simulation

	Acceptance criteria	This study
NMSE	< 1.5	0.01
FB	(-0.3,0.3)	-0.04
R	>0.8	0.99

770   **Table 2. Statics values of the 2D pollutant dispersion simulation**

	Acceptance criteria	This study
NMSE	< 1.5	0.06
FB	(-0.3,0.3)	-0.13
R	>0.8	0.95

775

Table 3. The description of all simulation cases

	Mechanism	Boundary conditions	Emissions	Wind condition
Base	Full	BC_NO_x = 20 ppbv; BC_VOCs = 40 ppbv; BC_O_3= 60 ppbv	E_NO_x = 4.37×10^{-8} kg m^{-3} s^{-1}; E_VOCs = 2.34×10^{-8} kg m^{-3} s^{-1}	U_{ref} = 3 m/s
Case_simple_mech	Simple	*Same as base*	*Same as base*	*Same as base*
Case_BC_zero	*Same as base*	BC_NO_x × 0; BC_VOCs × 0	*Same as base*	*Same as base*
Case_Emis_zero	*Same as base*	*Same as base*	E_NO_x × 0; E_VOCs × 0	*Same as base*
Case_Uref50%	*Same as base*	*Same as base*	*Same as base*	U_{ref} × 0.5
Case_Emis_Ctrl50%	*Same as base*	*Same as base*	E_NO_x × 0.5; E_VOCs × 0.5	*Same as base*
Case_Emis_Ctrl_VOCs20%	*Same as base*	*Same as base*	E_NO_x × 0.5; E_VOCs × 0.4	*Same as base*
Case_Emis_Ctrl_ VOCs30%	*Same as base*	*Same as base*	E_NO_x × 0.5; E_VOCs × 0.35	*Same as base*
Case_Emis_Ctrl_ VOCs40%	*Same as base*	*Same as base*	E_NOx × 0.5; E_VOCs × 0.3	*Same as base*